UNIVERSIDADE FEDERAL DO PARÁ
INSTITUTO DE GEOCIÊNCIAS
PROGRAMA DE PÓS-GRADUAÇÃO EM GEOLOGIA E GEOQUÍMICA

DISSERTAÇÃO DE MESTRADO Nº 687

ESTRUTURA VERTICAL E HOTSPOTS DE CARBONO: OS MANGUEZAIS AMAZÔNICOS ENTRE OS MAIS ALTOS DO MUNDO

Dissertação apresentada por:

ANGEE CATALINA CORTES BURGOS
Orientador: Prof. Dr. Marcelo Cancela Lisboa Cohen (UFPA)

BELÉM – PARÁ
2026

Dados Internacionais de Catalogação na Publicação (CIP) de acordo com ISBD Sistema de Bibliotecas da Universidade Federal do Pará
Gerada automaticamente pelo módulo Ficat, mediante os dados fornecidos pelo(a) autor(a)

C828e Cortes Burgos, Angee Catalina.
Estrutura vertical e hotspots de carbono: Os Manguezais amazônicos entre os mais altos do mundo. / Angee Catalina Cortes Burgos. — 2026.
79 f. : il. color.

Orientador(a): Prof. Dr. Marcelo Cancela Lisboa Cohen

Dissertação (Mestrado) - Universidade Federal do Pará, Instituto de Geociências, Programa de Pós-Graduação em Geologia e Geoquímica, Belém, 2026.

1. Manguezal. 2. Biomassa aerea. 3. Altura do dossel. 4. Stock de carbono. 5. Sensoramiento remoto. I. Título.

CDD 577.69809811

Universidade Federal do Pará
Instituto de Geociências
Programa de Pós-Graduação em Geologia e Geoquímica

ESTRUTURA VERTICAL E HOTSPOTS DE CARBONO: OS MANGUEZAIS AMAZÔNICOS ENTRE OS MAIS ALTOS DO MUNDO

Dissertação apresentada por

ANGEE CATALINA CORTES BURGOS

Como requisito parcial à obtenção de Grau de Mestre em Ciências na Área de GEOLOGIA e Linha de Pesquisa Geologia Marinha e Costeira.

Data de Aprovação: 13 / 03 / 2026

Banca Examinadora:

Prof. Dr. Marcelo Cancela Lisboa Cohen
(Orientador – UFPA)

Prof. Dr. André Rovai
(Membro - SERC)

Prof. Dr. Nils Edvin Asp Neto
(Membro-UFPA)

AGRADECIMENTOS

Quero agradecer aos meus pais, por terem me apoiado nesta jornada e por me proporcionarem a educação que tornou possível chegar até aqui. Em especial à minha mãe, por ser sempre a força amorosa que, dia após dia, me inspira e motiva por meio do seu exemplo.

Ao meu irmão Juan, por ser esse ser nobre, afetuoso, curioso e pacífico, que diariamente me ensina através de gestos de amor.

Ao meu orientador, Professor Dr. Marcelo Cohen, por ter me concedido a oportunidade de ampliar meus conhecimentos neste país extraordinário e pelos conselhos, orientação e acompanhamento ao longo do mestrado.

Às minhas amigas da Colômbia, Alejandra, Erika e Danna, pelo apoio incondicional durante todo esse percurso.

Aos amigos que conheci no Brasil e que fizeram da minha estadia uma das melhores fases da minha vida: Anita, Marlene, Juli, Marcial, Kike e Margorie.

Ao meu amigo Fernando, por ser um apoio constante e fundamental em todos os sentidos.

A Sergio Molano e Sebastian, pela valiosa ajuda e por serem guias importantes ao longo deste caminho.

Aos meus amigos e colegas de laboratório, Sérgio Nunes e Bettina, pelos conselhos, apoio e momentos compartilhados.

À Universidade Federal do Pará (UFPA), ao Instituto de Geociências e a todo o seu corpo técnico e administrativo, ao Programa de Pós-Graduação em Geologia (PPGG) e aos professores, que sempre demonstraram grande disposição para compartilhar e enriquecer o conhecimento que eu buscava, em especial aos professores Pedro Walfir, Laurent Polidori, Nils Asp e Marlon França.

Ao laboratório LADIC, pela infraestrutura, pelos equipamentos e pelo espaço disponibilizado para o desenvolvimento desta pesquisa.

Ao Brasil, ao estado do Pará, a sua cultura, e às suas pessoas maravilhosas, por me permitirem reconectar com a vida. Às árvores, ao mar e aos rios, pela sua força infinita.

O presente trabalho foi realizado com apoio da Coordenação de Aperfeiçoamento de Pessoal de Nível Superior – Brasil (CAPES), Código de Financiamento 001.

RESUMO

Os manguezais da costa amazônica brasileira desempenham um papel essencial no sequestro de carbono, na proteção costeira e na compreensão dos processos associados às mudanças climáticas. Entretanto, a estrutura vertical e a biomassa aérea dos manguezais do nordeste do estado do Pará, especialmente no Estuário do Rio Marapanim (ERM), ainda são pouco documentadas. Considerando que parâmetros alométricos como o diâmetro à altura do peito (DAP) e a altura do dossel (H) estão diretamente relacionados à biomassa aérea (AGB) e, portanto, aos estoques de carbono, este estudo teve como objetivo estimar a AGB e caracterizar os gradientes de altura do dossel no ERM. A pesquisa integrou medições de campo em duas zonas (Norte e Sul), levantamentos com veículos aéreos não tripulados (VANTs) e a identificação individual de árvores de *Rhizophora* e *Avicennia* a partir de imagens QuickBird. As alturas derivadas dos VANTs, combinadas com medições pontuais de DAP obtidas in situ, permitiram ajustar uma equação empírica baseada nos modelos alométricos. Além disso, foram integrados dados do Shuttle Radar Topography Mission (SRTM), do TanDEM-X e dos VANTs para comparar estimativas de biomassa em diferentes escalas e resoluções. Os resultados mostram que os manguezais do ERM apresentam indivíduos com mais de 49 m de altura, posicionando-se entre os mais altos já registrados globalmente. A biomassa máxima estimada por VANT alcançou aproximadamente 800 Mg/há, enquanto SRTM e TanDEM-X apresentaram valores inferiores (93 Mg/há e 136 Mg/há, respectivamente), refletindo diferenças associadas à resolução dos sensores, à densidade florestal, à heterogeneidade do dossel e à capacidade de cada modelo de identificar o topo do dossel. Em conjunto, os resultados indicam que os manguezais amazônicos brasileiros estão entre os mais altos e mais ricos em carbono do planeta, ressaltando sua relevância para o carbono azul, a mitigação climática e aplicações avançadas no sensoriamento remoto, incluindo a calibração de algoritmos satelitais de estimativa de biomassa.

Palavras-chave: manguezais amazônicos; biomassa aérea; altura do dossel; stock de carbono; sensoriamento remoto.

ABSTRACT

The mangroves of the Brazilian Amazon coast play a key role in carbon sequestration, coastal protection, and in improving our understanding of processes associated with climate change. However, the vertical structure and aboveground biomass (AGB) of mangroves in the northeastern sector of the state of Pará—particularly in the Marapanim River Estuary (ERM)—remain poorly documented. Considering that allometric parameters such as diameter at breast height (DBH) and canopy height (H) are directly related to AGB and, consequently, to carbon stocks, this study aimed to estimate AGB and to characterize canopy height gradients in the ERM. Field measurements conducted in two zones (North and South), combined with unmanned aerial vehicle (UAV) surveys, enabled the identification of individual Rhizophora and Avicennia trees using QuickBird imagery. UAV-derived canopy heights, together with in situ DBH measurements, allowed the development of an empirical equation based on the allometric models. Additionally, datasets from the Shuttle Radar Topography Mission (SRTM), TanDEM-X, and UAVs were integrated to compare biomass estimates across different spatial scales and sensor resolutions. The results indicate that mangroves in the ERM include individuals exceeding 49 m in height, placing them among the tallest mangroves ever recorded globally. Maximum biomass estimated from UAV data reached approximately 800 Mg/ha, whereas SRTM and TanDEM-X produced lower values (93 Mg/ha and 136 Mg/ha, respectively), reflecting differences associated with sensor resolution, forest density, canopy heterogeneity, and each model's ability to capture canopy-top elevations. Overall, these findings highlight the Brazilian Amazon mangroves as among the tallest and most carbon-rich on the planet, underscoring their importance for blue carbon, climate mitigation, and advanced remote sensing applications, including the calibration of satellite-based biomass estimation algorithms.

Keywords: Amazonian mangroves; aboveground biomass; canopy height, carbon stock; remote sensing.

LISTA DE ILUSTRAÇÕES

LISTA DE TABELAS

SUMÁRIO

1. INTRODUÇÃO

1.1 APRESENTAÇÃO

Desde a década de 1980, as áreas de manguezais vêm diminuindo a uma taxa média anual de aproximadamente 0,6% (Cardenas *et al.* 2022, Spalding *et al.* 2021). Apesar de sua distribuição global relativamente limitada de aproximadamente 13,6 milhões de hectares, restritos a zonas costeiras tropicais e subtropicais (Spalding *et al.* 2021), os manguezais oferecem benefícios ecológicos, sociais e econômicos (Alongi 2002). Esses ecossistemas atuam como barreiras naturais contra erosão costeira, tsunamis, inundações e furacões, desempenhando papel fundamental na proteção de áreas costeiras vulneráveis (Alongi 2002, 2008, 2015).

A estrutura florestal influencia diretamente a capacidade de proteção costeira (Chen *et al.* 2012, Das & Crépin 2013, Zhang *et al.* 2012).Variáveis estruturais como altura das árvores e diâmetro à altura do peito (DAP) também são fundamentais para estimar a biomassa aérea (AGB) e os estoques de carbono (Meng *et al.* 2021, Zaman *et al.* 2023). Manguezais mais altos tendem a armazenar maiores quantidades de carbono (Kauffman *et al.* 2020) com espécies como *Rhizophora* e *Avicennia* apresentando alto potencial de sequestro de carbono (Donato *et al.* 2011, Matos *et al.* 2020, Sanderman *et al.* 2019, Simard *et al.* 2019). Em escala global, estima-se que os manguezais armazenem entre 4 e 20 petagramas de carbono (Pg C) (Atwood *et al.* 2017, Jardine & Siikamäki 2014, Sanderman *et al.* 2018; Simard *et al.* 2019). O Brasil é o segundo maior detentor de estoques de carbono em manguezais, representando entre 7% e 8,5% do total global (Jardine & Siikamäki 2014, Rovai *et al.* 2022).

Apesar de sua relevância, a estimativa da altura do dossel e da biomassa aérea dos manguezais ainda enfrenta limitações tecnológicas significativas. Produtos orbitais amplamente utilizados, como o Shuttle Radar Topography Mission (SRTM) e o TanDEM-X, baseiam-se em interferometria radar nas bandas C e X, respectivamente, e não medem diretamente o topo real do dossel. A penetração do sinal radar na vegetação, aliada à resolução espacial relativamente grosseira (30 m para o SRTM e ~12 m para o TanDEM-X), resulta em suavização da superfície do dossel e subestimação sistemática da altura em florestas altas e estruturalmente heterogêneas. Esses erros estruturais se propagam diretamente às estimativas de biomassa e de carbono, especialmente em ecossistemas complexos como os manguezais amazônicos (Simard *et al.* 2025).

Tecnologias de sensoriamento remoto de alta resolução, como os veículos aéreos não tripulados (VANTs), têm se mostrado altamente eficazes na caracterização detalhada da estrutura do dossel, permitindo a identificação de copas emergentes, variações finas de altura e árvores individuais (Lagomasino *et al.* 2016, Simard *et al.* 2011). No entanto, na costa amazônica brasileira, estudos baseados em VANTs, capazes de fornecer dados de referência para a calibração e validação de produtos radar orbitais, ainda eram inexistentes.

Neste contexto, este estudo busca preencher uma lacuna tecnológica, ao integrar medições de campo, levantamentos com VANTs e dados orbitais do SRTM e do TanDEM-X para quantificar a altura do dossel, a densidade florestal e a biomassa aérea dos manguezais do nordeste do estado do Pará. Ao fornecer métricas estruturais de alta resolução espacial, este trabalho contribui para a calibração de algoritmos satelitais de estimativa de biomassa, reduzindo as incertezas associadas aos dados de radar e ampliando a confiabilidade dos mapas de carbono em manguezais tropicais. Esses avanços são essenciais para subsidiar estratégias de mitigação das emissões antrópicas de CO_2, ações de conservação e políticas públicas voltadas à proteção dos manguezais amazônicos.

1.2 AREA DE ESTUDO

A área de estudo localiza-se no estuário do rio Marapanim (ERM), na porção nordeste do estado do Pará, Brasil (0°51'41.05"S, 47°41'23.60"W) (Figura 1.1). A região está inserida na Reserva Extrativista Marinha Mestre Lucindo, unidade de conservação, e situa-se no domínio da Amazônia brasileira. O município de Marapanim encontra-se a aproximadamente 156 km da capital paraense, Belém, com acesso principal pela rodovia Castanhal–Curuçá.

O estuário do rio Marapanim está localizado aproximadamente 260 km a leste da foz do Rio Amazonas, integrando o amplo complexo estuarino amazônico. Sob o ponto de vista físico-geográfico, a área apresenta características típicas de ambientes estuarinos equatoriais, associados a costas dominadas por grandes sistemas fluviais da costa norte do Brasil (Berrêdo *et al.* 2008, Matos *et al.* 2020, Vilhena *et al.* 2010).

1.3 OBJETIVOS

Avaliar a estrutura vertical do dossel e a biomassa aérea (AGB) dos manguezais do Estuário do Rio Marapanim (nordeste do estado do Pará), integrando dados de campo, levantamentos com veículos aéreos não tripulados (VANTs) e produtos orbitais de radar (SRTM e TanDEM-X), com o objetivo de identificar e reduzir limitações tecnológicas associadas à estimativa da altura do dossel e da biomassa em manguezais altos e estruturalmente heterogêneos.

1.3.1 Objetivos específicos

1. Caracterizar a estrutura vertical do dossel dos manguezais do Estuário do Rio Marapanim, quantificando a altura das árvores e os gradientes espaciais de altura em diferentes setores do estuário.
2. Estimar a biomassa aérea (AGB) dos manguezais a partir da integração entre medições de campo do diâmetro à altura do peito (DAP) e alturas do dossel derivadas de VANTs, utilizando modelos alométricos empíricos.
3. Comparar as estimativas de altura do dossel e biomassa aérea obtidas por VANTs com aquelas derivadas de produtos orbitais de radar (SRTM e TanDEM-X), avaliando diferenças associadas à resolução espacial, à penetração do sinal radar e à heterogeneidade estrutural da floresta.
4. Quantificar os vieses e limitações tecnológicas dos dados de radar interferométrico na estimativa da altura do dossel e da biomassa aérea em manguezais altos e complexos.
5. Avaliar o papel dos VANTs como dados de referência para calibração e validação de produtos orbitais, contribuindo para a melhoria de algoritmos satelitais de estimativa de biomassa em ecossistemas costeiros tropicais.
6. Discutir as implicações dos resultados para a estimativa de estoques de carbono azul, para estratégias de mitigação das emissões de CO_2 e para o aprimoramento do uso do sensoriamento remoto no monitoramento de manguezais amazônicos.

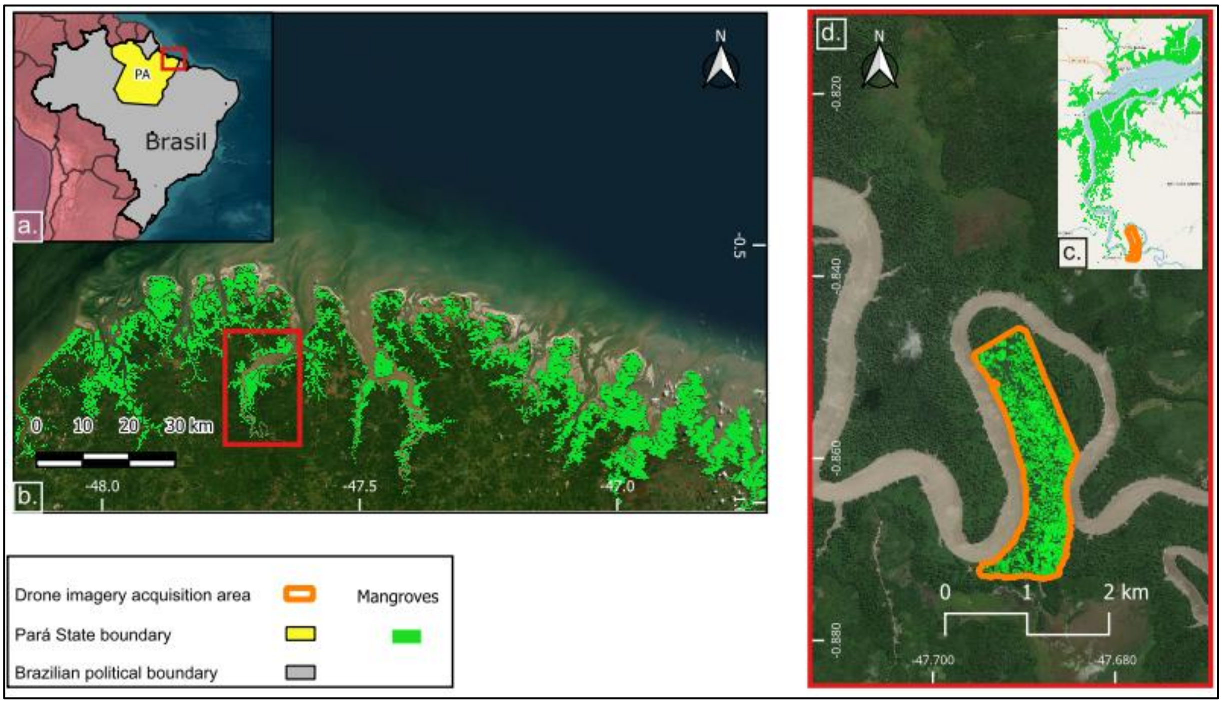

Figura 1.1- a. Localização da área de Estudo no Brasil; b. Cobertura do mangue ao longo da Costa Amazônica; c. Estuário do Rio Marapanim; d. Area de sobrevoo do drone.

1.4 MÉTODOS

O uso de veículos aéreos não tripulados (VANTs) tornou-se uma ferramenta confiável para estimar a biomassa aérea e analisar as características estruturais da vegetação arbórea

(Castellanos-Galindo *et al.* 2021, Navarro *et al.* 2020, Panagiotidis *et al.* 2017). Este estudo adotou uma abordagem integrada de sensoriamento remoto e validação em campo para a caracterização estrutural dos manguezais do Estuário do rio Marapanim e a estimativa da biomassa aérea com uma integração de dados do Shuttle Radar Topography Mission (SRTM), imagens orbitais do TanDEM-X, levantamentos aerofotogramétricos com veículos aéreos não tripulados (VANTs) e medições topográficas e de Diâmetro à Altura do Peito (DAP-DBH) obtidas em campo. Estudos prévios têm demonstrado o potencial dos veículos aéreos não tripulados (VANTs) na investigação da estrutura dos manguezais. Hsu *et al.* (2020) compararam dados do Global Mangrove Watch (GMW) com levantamentos aéreos, destacando o valor complementar dos drones no monitoramento dos manguezais.

As campanhas de campo incluíram medições com receptor GNSS diferencial Trimble Catalyst, apoiadas por levantamentos relativos de altitude com teodolito eletrônico, utilizadas para validação dos modelos digitais de elevação e das alturas de dossel. Os levantamentos com VANT foram realizados em outubro de 2024 e 2025, empregando um drone DJI Phantom 4

Advanced equipado com sistema GPS, sensores inerciais e uma câmera RGB FC6310 (4K/20 MP, distância focal de 8,8 mm, largura do sensor de 12,8 mm, 5472 pixels).

A metodologia geral foi estruturada em quatro etapas (Fig. 1.2): **(1)** Análise regional com base em dados SRTM e de satélite; **(2)** Avaliação em escala local a partir de medições de campo e dados de alta resolução obtidos por drone; **(3)** Integração dos dados em análises estatísticas; e **(4)** Geração de modelos de biomassa aérea para os manguezais.

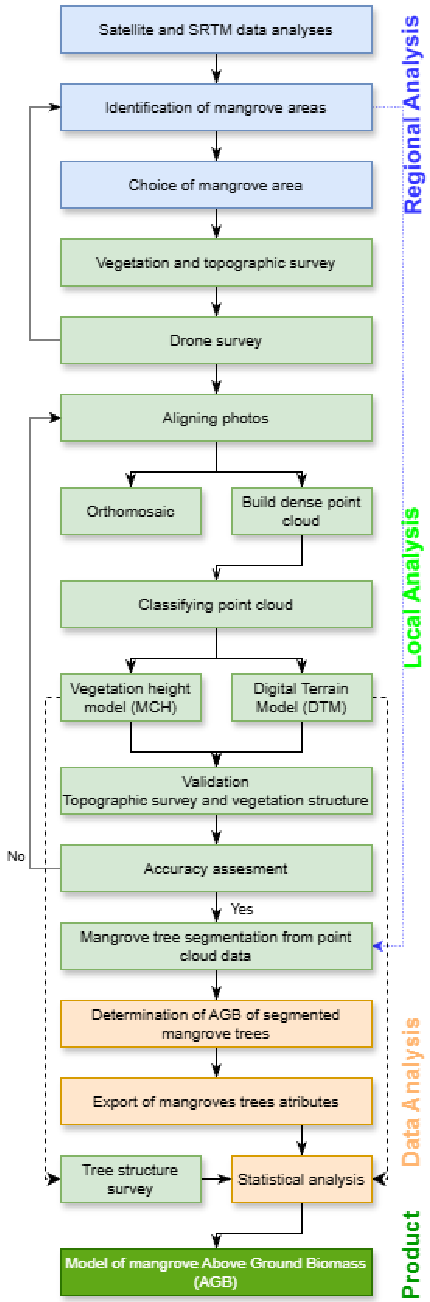

Figura 1.2- Fluxograma de trabalho

1.4.1 Análise regional com base em dados de satélite e SRTM

Imagens multiespectrais QuickBird, com resolução espacial de 2,44 m (bandas azul, verde e vermelha), disponibilizadas no Google Earth, foram empregadas para o mapeamento dos manguezais ao longo do estuário do rio Marapanim. A classificação da cobertura do solo foi realizada por interpretação visual no software Global Mapper, resultando na distinção de seis classes principais: manguezal, vegetação herbácea, planície lamosa, planície arenosa, corpos d’água e áreas antropizadas. A interpretação visual fundamentou-se na heterogeneidade estrutural dos manguezais e na sobreposição espectral observada nas imagens.

Os gêneros *Avicennia* e *Rhizophora* foram mapeados individualmente considerando diferenças de tonalidade, textura e arranjo espacial do dossel. Para a caracterização altimétrica em escala regional, utilizou-se o Modelo Digital de Elevação da Shuttle Radar Topography Mission (SRTM), processado em formato GeoTIFF no software Global Mapper. As altitudes derivadas do SRTM, obtidas por interferometria de radar, correspondem a alturas ortométricas referidas ao geoide EGM96.

Considerando que os manguezais se desenvolvem em cotas próximas ao nível médio do mar e que, na área de estudo, distribuem-se entre –2 m e 3 m acima desse nível, as elevações do SRTM sobre áreas vegetadas foram interpretadas como uma aproximação da altura média do dossel. A amostragem das elevações foi realizada diretamente sobre as copas das árvores previamente digitalizadas, por meio da ferramenta *Apply Elevations to Selected Features*.

A estimativa da biomassa aérea (AGB) baseou-se em dados estruturais obtidos em campo, incluindo medições de Diâmetro à Altura do Peito (DAP) e altura das árvores. Para *Rhizophora*, aplicou-se a equação alométrica proposta por Komiyama *et al.* (2008), enquanto para *Avicennia* adotou-se a formulação pantropical de Chave *et al.* (2005), que incorpora a densidade da madeira (ρ) e apresenta robustez para árvores tropicais de grande porte. A escolha desta última deveu-se à ausência de equações específicas validadas para indivíduos de *Avicennia* com alturas superiores a 30 m.

A partir da biomassa estimada com base nos DAPs medidos em campo, foram ajustados modelos empíricos relacionando altura e AGB para cada gênero. Os modelos de melhor desempenho estatístico (R^2 e RMSE) foram posteriormente aplicados às árvores mapeadas por sensoriamento remoto, permitindo a estimativa espacialmente explícita da biomassa aérea ao longo do estuário.

1.4.2 Análise local com drone

As imagens de alta resolução adquiridas com o DJI Phantom 4 Advanced, equipado com uma câmera RGB FC6310 Montada em um gimbal com compensação de movimento, produziu imagens com uma resolução espacial (GSD) de 2,6 cm/pixel a uma altitude de voo de 100 m, calculada conforme a equação:

$$GSD = \frac{Sw * H * \frac{100}{60}}{(Fr * imH)} \qquad (1)$$

onde *Sw* é a largura do sensor (mm), *H* a altura de voo (m), *Fr* a distância focal (mm) e *imH* a largura da imagem (pixels) (PIX4D, 2013).

Os levantamentos aerofotogramétricos com veículos aéreos não tripulados (VANTs) foram planejados no software DJI Ground Station Pro, com definição prévia de pontos de passagem, câmera orientada em nadir (90°) e sobreposição de 90% no sentido longitudinal e 80% no sentido lateral. As missões foram realizadas em outubro de 2024 e 2025, cobrindo aproximadamente 912 ha de manguezais, com cada missão mapeando cerca de 48 ha por voo, em função da autonomia das baterias (17–20 minutos).

Na área sul, foram adquiridas 1.705 imagens, posteriormente processadas no software Agisoft Metashape v2.1.1, utilizado para a geração do ortomosaico, da nuvem densa de pontos e dos modelos digitais de elevação. Além dos voos nadirais, foram executadas missões específicas de fotogrametria circular ao redor de árvores selecionadas, com planos de voo programados para manter altitude constante (30–60 m), raio entre 60 e 120 m e orientação oblíqua da câmera (45°). Essa estratégia permitiu a aquisição de imagens sobrepostas a partir de múltiplas perspectivas, favorecendo a reconstrução tridimensional das copas e a redução de zonas de oclusão. As missões foram conduzidas com sobreposição mínima de 80%, assegurando redundância adequada para o processamento fotogramétrico por *Structure-from-Motion* (SfM) e a posterior derivação da altura das árvores e da morfologia do dossel.

1.4.3 Pontos de controle em solo (GCPs)

As medições foram realizadas com uma antena Trimble Catalyst operando em modo GNSS diferencial, alcançando precisão planimétrica da ordem de ±30 cm após o período de estabilização. Esses pontos foram utilizados como referência para o levantamento topográfico com teodolito eletrônico CST Berger DGT10, a partir do qual foram determinadas as elevações relativas dos Pontos de Controle em Solo (GCPs), com precisão altimétrica de aproximadamente ±10 cm.

As alturas elipsoidais obtidas foram convertidas para alturas ortométricas com base no modelo de geoide SIRGAS2000 do IBGE. No total, vinte GCPs foram utilizados na calibração do Modelo Digital de Elevação derivado da fotogrametria. As alturas das árvores de mangue foram medidas em campo com inclinômetro de laser. Adicionalmente, quatro parcelas de 100 × 100 m foram inventariadas para a caracterização da densidade arbórea, altura e diâmetro à Altura do Peito (DAP), fornecendo validação do modelo de altura da vegetação obtido a partir dos dados de VANT.

1.4.4 Geração e validação de modelos 3D

As imagens obtidas por drone em outubro de 2024 e 2025 foram processadas no software Agisoft Metashape Professional (v. 2.2.0) por meio da técnica de fotogrametria Structure-from-Motion (SfM) (Xu *et al.*, 2018), permitindo a geração de ortomosaicos, Modelos Digitais de Superfície (MDS) e nuvens densas de pontos com espaçamento médio entre 3 e 5 cm. Todo o processamento foi referenciado espacialmente com base nos Pontos de Controle em Solo (GCPs) obtidos com o receptor Trimble Catalyst DA2 e teodolito eletrônico.

Inicialmente, as nuvens esparsas foram filtradas segundo critérios de erro de reprojeção, incerteza de reconstrução, número de imagens e precisão de projeção, resultando em aproximadamente 2 milhões de pontos confiáveis distribuídos sobre uma área de 912 ha. Em seguida, foram geradas nuvens densas contendo cerca de 15 milhões de pontos, posteriormente validadas com os 20 GCPs levantados em campoDados de elevação e espectrais de 2.000 pontos amostrais foram extraídos no Global Mapper e analisados estatisticamente; a classificação baseada em atributos RGB e elevação permitiu distinguir formações de Avicennia e Rhizophora da vegetação adjacente e das feições geomorfológicas. Os resultados da classificação foram comparados com ortomosaicos obtidos por drone e validados por meio de fotografias panorâmicas e dados de campo.

A partir da classificação da nuvem de pontos, os pontos atribuídos à classe Ground foram utilizados para a geração do Modelo Digital do Terreno (MDT) por meio da ferramenta *Create Elevation Grid from 3D Vector/LiDAR Data* no software Global Mapper. De forma análoga, o Modelo Digital de Superfície (MDS) foi produzido a partir das classes de vegetação baixa, média e alta. O Modelo de Altura do Dossel (CHM) foi então obtido pela subtração do MDT em relação ao MDS, conforme a expressão:

$$CHM = MDS - MDT \tag{2}$$

seguindo o procedimento descrito por Cohen *et al.* (2024), implementado com a ferramenta *Combine/Compare Terrain Layers*.

Os Modelos Digitais de Elevação (MDE) foram gerados no Global Mapper utilizando o método de *binning* (10 pontos, espaçamento aproximado de 2 cm) com filtro de valor máximo. A acurácia vertical foi avaliada por meio da comparação entre as elevações do MDT e os GCPs, resultando em erros verticais inferiores a 20 cm, dentro da tolerância de ±30 cm associada aos dados GNSS do Catalyst.

Dados espectrais (RGB) e altimétricos de 2.000 pontos amostrais foram extraídos no Global Mapper e analisados estatisticamente, permitindo a distinção entre formações dominadas por *Avicennia* e *Rhizophora*, bem como a separação da vegetação adjacente e de feições geomorfológicas. Os resultados da classificação foram verificados por meio da comparação com ortomosaicos de alta resolução, fotografias panorâmicas e observações de campo.

Adicionalmente, missões circulares com drone ao redor de árvores individuais permitiram a geração de nuvens tridimensionais de alta densidade, capturando a geometria do tronco e dos principais ramos. Esses modelos foram processados em ambiente MATLAB para estimativa volumétrica dos componentes lenhosos, possibilitando a quantificação da biomassa aérea em escala individual.

1.4.5 Segmentação de árvores de mangue

A nuvem de pontos densa foi processada e classificada no software Global Mapper Pro (versão 26.1), utilizando as ferramentas integradas de classificação de dados 3D para diferenciar as classes de solo (Ground) e vegetação (Vegetation), subdividida em vegetação baixa, média e alta (*Low, Medium e High Vegetation*).

A partir da nuvem classificada, procedeu-se à segmentação de árvores individuais dos gêneros *Avicennia* e *Rhizophora*, com o objetivo de extrair métricas estruturais em nível de indivíduo, estimar a densidade arbórea por hectare e calcular a biomassa aérea (*aboveground biomass*). O Modelo de Altura do Dossel (CHM) de alta resolução, foi utilizado para a detecção de máximos locais, que serviram como pontos-semente no processo de segmentação das copas dentro das formações de mangue previamente classificadas por gênero.

A individualização das árvores foi realizada com a ferramenta *Automatic Point Cloud Analysis*, parametrizada com base em dados de campo e inspeção visual, considerando resolução espacial de 2 m, espalhamento mínimo de copa de 5 m e máximo de 40 m, altura mínima acima do solo de 5 m, limiar de vegetação média de 20 m e limiar de vegetação alta de até 52 m. Para cada agrupamento de copa identificado, a altura da árvore foi estimada como a diferença entre o ponto mais elevado da copa e a elevação correspondente do Modelo Digital do Terreno (MDT).

Durante o processo de segmentação, foram excluídas unidades de vegetação com altura inferior a 10 m, a fim de evitar a inclusão de arbustos (~5 m) e palmeiras com alturas entre 10 e 15 m, cuja morfologia e estrutura não correspondem a indivíduos típicos de mangue. Essa filtragem contribuiu para reduzir ruídos na quantificação estrutural da floresta.

A densidade arbórea foi estimada por meio da ferramenta *Create Density Grid*, que gerou um raster de densidade de árvores por hectare. Os resultados obtidos automaticamente foram validados por contagens manuais realizadas sobre os ortomosaicos de alta resolução obtidos por VANT, assegurando a consistência da segmentação e das estimativas derivadas.

1.4.6 Integração e análise dos dados

Foi realizada uma análise estatística comparativa para avaliar a consistência entre as medições de elevação, altura das árvores e biomassa aérea (AGB) obtidas em campo e aquelas derivadas dos dados de drone. Foram aplicadas regressões lineares para cada variável, e o ajuste dos modelos foi avaliado por meio do coeficiente de determinação (R^2) como principal métrica de desempenho. A precisão dos modelos também foi quantificada utilizando três métricas de erro: viés (BIAS), erro absoluto médio (MAE) e raiz do erro quadrático médio (RMSE), calculadas de acordo com as seguintes equações:

$$BIAS = \frac{1}{n} * \sum_{i=1}^{n} (x_i - y_i) \quad (3)$$

$$MAE = \frac{1}{n} * \sum_{i=1}^{n} |(x_i - y_i)| \quad (4)$$

$$RMSE = \sqrt{\frac{1}{n} * \sum_{i=1}^{n} (x_i - y_i)^2} \quad (5)$$

Onde x_i representa os valores obtidos pelas medições realizadas com o drone, e y_i representa os valores obtidos diretamente nas medições de campo das árvores.

1.4.7 Estimativa alométrica da biomassa aérea (AGB)

A biomassa aérea (AGB) de *Rhizophora* e *Avicennia* foi estimada a partir de medições de campo do diâmetro à altura do peito (DAP) e da altura das árvores, utilizando equações alométricas baseadas exclusivamente em DAP e densidade da madeira (ρ). Para *Rhizophora*, aplicou-se a equação específica para manguezais proposta por Komiyama *et al.* (2008), enquanto para *Avicennia* foi utilizada a formulação pantropical de Chave *et al.* (2005). Essa escolha deve-se à ausência de equações específicas validadas para *Avicennia* com alturas entre 30 e 50 m, sendo o modelo de Chave *et al.* (2005) amplamente empregado para árvores tropicais de grande porte (≈10–60 m).

No total, foram amostradas 63 árvores (30 de *Rhizophora* e 33 de *Avicennia*) distribuídas nos setores norte e sul da área de estudo. O DAP foi medido a 1,3 m do solo, e a altura (H) determinada em campo com clinômetro, com georreferenciamento realizado por GPS portátil. As alturas medidas foram posteriormente comparadas às estimativas obtidas a partir dos modelos digitais de terreno e superfície (DEM/DSM; CHM = DSM–DEM), garantindo a consistência entre os dados de campo e os produtos derivados por sensoriamento remoto.

A partir das estimativas de AGB baseadas no DAP, foram ajustadas regressões empíricas entre altura (H) e AGB, separadamente para *Avicennia* e *Rhizophora*. O modelo de melhor desempenho foi selecionado com base em métricas estatísticas (R^2 e RMSE) e posteriormente aplicado para estimar a biomassa aérea individual das árvores delineadas nas imagens de satélite, utilizando as alturas extraídas.

A biomassa aérea foi estimada utilizando alometrias que empregam apenas DAP e densidade da madeira (ρ), com fontes específicas por espécie:

- **Rhizophora** (Komiyama *et al.*, 2008; modelo geral para manguezais):

$$AGB = 0.251 \times \rho \times DAP^{2.46} \quad (6)$$

- **Avicennia** (Chave *et al.*, 2005; floresta úmida, modelo com ρ):

$$AGB = \rho\, e^{-1.499 + 2.148 \ln D + 0.207 (\ln D)^2 - 0.0281 (\ln D)^3} \quad (7)$$

Foram utilizados valores de densidade da madeira obtidos na literatura (**ρ = 0,90 g/cm³ para Rhizophora e 0,74 g/cm³ para Avicennia**), representativos das espécies dominantes no local. com base em compilações globais amplamente utilizadas, como a base de dados de densidade da madeira de Zanne *et al.* (2009).

As estimativas individuais de biomassa aérea (AGB) foram empregadas para: (1) Avaliar a concordância entre as alturas medidas em campo e aquelas derivadas do Modelo de Altura do Dossel (CHM); e (2) Calibrar e validar a relação empírica altura–AGB utilizada no mapeamento contínuo da biomassa na área de estudo.

O diâmetro à altura do peito (DAP) foi medido com precisão de 0,1 cm, enquanto a altura das árvores foi obtida com precisão de 0,5–1 m. Valores discrepantes em relação ao CHM foram verificados por meio de uma tolerância de ±2–3 m, com remedição em campo quando necessário. As coordenadas foram registradas no sistema UTM do projeto, com acurácia horizontal do GPS geralmente ≤5–7 m em áreas com abertura do dossel.

A seleção das equações alométricas considerou os intervalos de porte e altura para os quais cada modelo foi originalmente desenvolvido e validado. Para *Rhizophora*, adotou-se a equação específica para manguezais proposta por Komiyama *et al.* (2008), adequada a árvores de médio a grande porte observadas na área. Para *Avicennia*, a inexistência de modelos específicos calibrados para indivíduos muito altos (≈30–50 m) levou à utilização da equação pantropical de Chave *et al.* (2005), que incorpora a densidade da madeira e apresenta desempenho consistente em diferentes formações florestais e classes de tamanho, minimizando vieses associados à extrapolação alométrica.

2. FUNDAMENTAÇÃO TEÓRICA

Os manguezais do nordeste do estado do Pará integram o cinturão de manguezais mais contínuo do mundo, distribuindo-se ao longo de ambientes estuarinos e de inlets desde a foz do rio Amazonas até o estado do Maranhão (Nascimento *et al.* 2013). Esses ecossistemas constituem zonas de transição entre ambientes florestais e sistemas costeiros, sendo fortemente influenciados pela hidrografia amazônica e pela elevada pluviosidade, que conferem importante aporte de água doce (Fernandes 2016).

Na região, os manguezais abrigam uma ampla biodiversidade de plantas, peixes, aves, répteis, anfíbios, mamíferos e macroinvertebrados marinhos e terrestres, refletindo a complexidade ecológica desses ambientes (Fernandes 2016).

A seguir, apresenta-se uma síntese das condições geológicas, geomorfológicas, oceanográficas e estruturais relacionadas aos manguezais da área de estudo.

2.1 CONTEXTO GEOLÓGICO E GEOMORFOLÓGICO

2.1.1 Geologia

O estuário do Rio Marapanim está localizado sobre depósitos do Neógeno e do Paleogeno, correspondentes aos sedimentos pós-Barreiras e Formação Barreiras (ENb) (Silva *et al.*, 2009). A Formação Barreiras (ENb) é constituída por conglomerados com intercalações de areias e argilas (Rosseti *et al.*, 1989), além disso, fornece nesta área siltes, quartzo e oxi-hidróxidos de ferro (Berrêdo *et al.*, 2008). Os sedimentos pós-Barreiras são de idade holocênica e consistem em depósitos sedimentares areio-argilosos (C. Silva, 1998). A zona de estudo encontra-se sobre os depósitos recentes pós-Barreiras, correspondentes aos Depósitos Aluvionares e Depósitos Litorâneos. Nos manguezais, os sedimentos são constituídos principalmente por silte, seguidos de argila, e uma proporção menor de areia. Também é comum encontrar restos de folhas, raízes, conchas e diatomáceas (Berrêdo *et al.*, 2008).

2.1.2 Geomorfología

Segundo Silva (2009), a geomorfologia da área de estudo é composta por planície costeira, estuarina e aluvial (figura 2.1). A planície costeira é formada por depósitos de areia e argila e possui oito unidades geomorfológicas: paleoduna, duna costeira, pântano salino, planície de maré, lago, antigo canal de maré, planície de cristas de praia e praia flecha-barreira. A planície estuarina é caracterizada por processos marinhos e apresenta três unidades morfológicas: canal estuarino, canal de maré e planície de inundação. A planície aluvial é comumente inundada pelas águas que transbordam do canal meandrante, sendo posteriormente drenada pelo Rio Marapanim. Isso favorece a deposição dos sedimentos areio-argilosos da Formação Barreiras. As unidades geomorfológicas presentes incluem: canal meandrante, depósitos de canal, depósitos de margens de canal, depósitos de preenchimento de canal. A zona de estudo no estuário corresponde a uma planície meandrante composta por estratos alternados de areia fina e lama (Silva *et al.*, 2009), onde predominam manguezais de zona de intermarés (Silva, 1998).

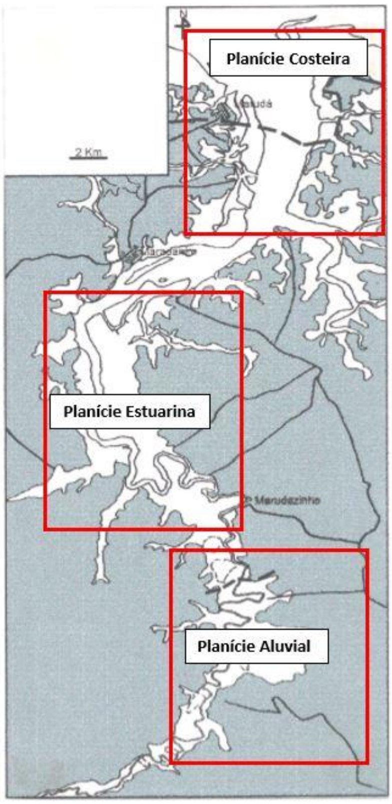

Figura 2.1- Geomorfologia do estuário do Rio Marapanim. Modificado de Silva (1998).

Na área de estudo, observa-se a presença de numerosos canais de maré, típicos de sistemas estuarinos de macromarés, que atuam como vias bidirecionais de transporte de sedimentos e nutrientes entre o ambiente marinho e o continente (Wang *et al.*, 2021). A eficiência desses fluxos depende diretamente da conectividade hidrodinâmica e da dinâmica das marés (McLachlan *et al.*, 2020). De modo geral, a sedimentação em estuários concentra-se em planícies de inundação, com predomínio de material fino e intercalações de camadas arenosas (Bird, 2008; Woodroffe *et al.*, 2016), padrão claramente observado no ERM e fundamental para a manutenção da estrutura geomorfológica e ecológica dos manguezais locais.

2.1.3 Origem do mangue no ERM e variações no nível do mar

Na costa amazônica do Brasil, o estabelecimento e a expansão dos manguezais estão intimamente associados às variações do nível relativo do mar e às oscilações climáticas ao longo do Holoceno. Registros paleoecológicos indicam que os primeiros manguezais se desenvolveram durante o Holoceno inicial e médio, em resposta a fases de transgressão marinha que favoreceram a inundação costeira e a intrusão salina em áreas anteriormente continentais (Cohen, *et al.*, 2005a; Cohen, *et al.*, 2005b; Behling, 2002). Esses processos foram modulados por alternâncias entre períodos climáticos mais secos e mais úmidos, que controlaram o equilíbrio entre o aporte fluvial, a sedimentação e a salinidade costeira (Cohen *et al.*, 2012). Evidências provenientes de áreas adjacentes, como o Lago Crispim, indicam a presença de manguezais entre aproximadamente 7.550 e 6.620 anos AP, com fases sucessivas de expansão e retração vinculadas tanto às flutuações do nível do mar quanto a condições climáticas mais úmidas, favoráveis ao desenvolvimento dessas formações vegetais (Behling, 2002; Pessenda *et al.*, 2004). Em conjunto, esses registros demonstram que os manguezais amazônicos são ecossistemas dinâmicos, cuja distribuição e estrutura atuais refletem uma longa história de interação entre forçantes eustáticas, climáticas e sedimentares.

2.2 OCEANOGRAFIA

Segundo Silva *et al.* (2009) a zona de estudo encontra-se influenciada por um regime de macromarés com marés semidiurnas, com uma amplitude que varia entre 3,5 m durante marés mortas e até 6 m em marés vivas. O efeito da maré pode influenciar o estuário até 70 km rio acima. A salinidade aumenta ao longo do estuário, variando entre 29‰ e 1‰, em direção ao interior. O período de baixa precipitação pluvial caracteriza-se pelo domínio das correntes de marés e as águas salgadas chegam a penetrar mais de 60 km no estuário. A salinidade atinge sua amplitude máxima, próxima de 35 ‰. No período de maior descarga fluvial os valores de salinidade caem, atingindo valores de até 3‰ na área de Marapanim, e 0‰ na área sul da zona de estudo.

As correntes no nordeste do Pará são controladas principalmente pelas marés, com velocidades de até 1,43 m/s, e pelos ventos alísios de nordeste (5–10 m/s), que geram deriva litorânea para o noroeste. Esses processos são os principais responsáveis pelo transporte e pela redistribuição de sedimentos na região costeira do estuário do rio Marapanim. (Silva *et al.*, 2009).

2.3 ESPÉCIES DE MANGUE

Em termos biogeográficos, *A. germinans* apresenta ampla distribuição no continente americano: desde as Bermudas até o sudeste do Brasil, no Atlântico, e do México até o Peru, no Pacífico (Lacerda *et al.*, 2002), sendo particularmente comum na costa norte do Brasil, onde ocorre em áreas de maior salinidade (Machado *et al.*, 2008). As espécies de mangue presentes na Plataforma Continental Norte Brasileira (PCNB) totalizam seis: duas de mangue-preto (*Avicennia germinans* e *A. schaueriana*), três de mangue-vermelho (*Rhizophora mangle*, *R. racemosa* e *R. harrisonii*), e uma de mangue-branco (*Laguncularia racemosa*). Entre elas, *Avicennia germinans* destaca-se por seu rápido crescimento e por ser uma das espécies mais altas e predominantes da região, ocupando amplas faixas do litoral norte brasileiro (Fernandes *et al.*, 2025). Na Amazônia brasileira, diversos estudos relatam a coexistência de *A. germinans* e *Rhizophora* (Cardenas *et al.*, 2022; Lara & Cohen, 2006; Menezes *et al.*, 2008; Pamplona *et al.*, 2013). No ERM, *A. germinans* concentra-se próximo à desembocadura, especialmente nas zonas mais elevadas (Berredo *et al.*, 2008; Matos *et al.*, 2020).

2.4 ESTRUTURA DO MANGUE

A altura é um parâmetro estrutural fundamental, amplamente associado à biomassa e ao estoque de carbono em manguezais (Aslan *et al.*, 2022). Como o crescimento ocorre em todas as partes da árvore, métricas como a altura e o diâmetro à altura do peito (DAP) estão diretamente relacionadas ao seu peso e, consequentemente, à biomassa total (Komiyama *et al.*, 2008). A biomassa aérea (AGB) representa um indicador essencial para estimar o sequestro de carbono e o potencial de mitigação das mudanças climáticas (Osland *et al.*, 2014), apresentando tendência de aumento em direção ao interior continental em comparação com as zonas mais próximas ao mar (Komiyama *et al.*, 2008). Assim, o DAP constitui um parâmetro estrutural fortemente correlacionado à biomassa, pois reflete a quantidade de tecido biomecânico e condutor necessária para sustentar e conectar os fluxos de recursos entre as partes aérea e subterrânea da planta (Price *et al.*, 2024). As equações alométricas que integram densidade da madeira, altura e DAP são amplamente reconhecidas como os preditores mais robustos de biomassa (Chave *et al.*, 2005).

No ERM, os indivíduos de maior altura de *Avicennia germinans* concentram-se predominantemente nas porções mais internas do manguezal, onde são reconhecidos como alguns dos exemplares mais senescentes da região (Berredo *et al.*, 2008; Matos *et al.*, 2020). Essa espécie apresenta elevada tolerância a salinidade extrema (Lagomasino *et al.*, 2021; Matos *et al.*, 2023); contudo, em ambientes de baixa salinidade, alcança taxas de crescimento significativamente superiores, ajustando sua fisiologia por meio da redução do crescimento sob estresse salino, como estratégia para a manutenção do equilíbrio osmótico (Ball, 1988; Cohen & Lara, 2006; Suárez & Medina, 2005).

2.5 STOCK DE CARBONO E MUDANÇAS CLIMÁTICAS

Os manguezais são reconhecidos como importantes sequestradores de carbono, o que os torna elementos de grande valor nas estratégias de adaptação e mitigação das mudanças climáticas (Kauffman *et al.* 2020). A estimativa do carbono armazenado é considerada de grande importância, pois permite avaliar a contribuição dos manguezais para a regulação do clima (Peñaranda *et al.* 2019). Uma parte considerável do carbono capturado pelos manguezais é armazenada no solo, o que é considerado positivo, já que se o carbono está retido no solo, pode permanecer sequestrado por milênios, enquanto se estiver na biomassa, só pode ser armazenado por décadas (Suresh & Soon Park 2018). Entre as espécies de mangue que podem armazenar maiores quantidades de carbono estão *Rhizophora* e *Avicennia*. Esses gêneros podem apresentar estaturas entre as mais altas dos manguezais (Kauffman *et al.* 2020). A altura do dossel nos manguezais está fortemente relacionada à rotatividade do carbono, por meio da produção e da queda de folhas, um fator crucial para avaliar a produtividade do solo e as taxas de sequestro de carbono mencionadas (Simard *et al.* 2019). Dado que existe uma relação entre a altura e o armazenamento de carbono acima do solo, essa altura pode funcionar como indicador de alterações devido às mudanças climáticas, bem como para captura de carbono (Ghosh *et al.* 2020).

Os manguezais são ecossistemas particularmente vulneráveis às mudanças climáticas, uma vez que sua persistência depende do equilíbrio entre a taxa de acumulação de sedimentos e a elevação do nível do mar. Quando a sedimentação ocorre a uma taxa inferior ao aumento do nível do mar, os manguezais perdem a capacidade de se ajustar verticalmente, tornando-se suscetíveis à submersão e à degradação progressiva de seus habitats (Gilman *et al.* 2008). Projeções do Painel Intergovernamental sobre Mudanças Climáticas (Ipcc 2007) indicam que, até o ano de 2100, o nível médio global do mar poderá elevar-se em aproximadamente 30 cm, com impactos diretos sobre a distribuição, a estrutura e a sobrevivência das espécies de mangue, em função do aumento do período e da profundidade das inundações (Lu *et al.* 2013).

Nesse contexto, as árvores de mangue constituem importantes bioindicadores das variações do nível do mar, uma vez que apresentam respostas fisiológicas e estruturais sensíveis às mudanças nas condições costeiras (Blasco *et al.*, 1996). A elevação do nível do mar implica alterações nos regimes de salinidade e de inundação dos ambientes estuarinos, afetando o balanço hídrico e os processos ecofisiológicos das plantas, o que pode resultar em estresse, redução do crescimento e, em cenários extremos, no colapso dos ecossistemas de manguezal (Unep 1994).

3. RESULTADOS - Artigo

Artigo em julgamento na *International Journal of Applied Earth Observation and Geoinformation* (IF 8.6)

3.1 ARE AMAZONIAN MANGROVES AMONG THE TALLEST GLOBALLY? INSIGHTS FROM UAV AND SATELLITE OBSERVATIONS

Angee C. C. Burgos[a], Marcelo C. L. Cohen[a,b*], Sergio P. Nunes[a], Luiz C.R. Pessenda[c]

[a] Graduate Program of Geology and Geochemistry, Federal University of Pará. Av. Perimentral 2651, Terra Firme, 66077-530, Belém (PA), Brazil.
[b]Department of Oceanography and Coastal Sciences, Louisiana State University, Baton Rouge, Louisiana 70803, USA
[c] University of São Paulo, CENA/^{14}C Laboratory, Av. Centenário 303, 13400-000, Piracicaba, São Paulo, Brazil.

Corresponding authors:
*Marcelo Cancela Lisboa Cohen
Federal University of Pará - Brazil
Rua Augusto Corrêa, 01 - Guamá. CEP 66075-110, Belém (PA), Brazil.
Tel.: +55 91 3201-7988
E-mail address: mcohen80@hotmail.com

Angee Catalina Cortes Burgos

Tel: +57 3213693081

E-mail address: angee.burgos@ig.ufpa.br

ABSTRACT

Mangroves along the Amazon-influenced coast are among the most carbon-rich coastal ecosystems globally, yet their vertical structure and above-ground biomass (AGB) remain poorly constrained by current Earth observation (EO) products. Here, we integrate ultra–high-resolution UAV-based photogrammetry with TanDEM-X and SRTM digital elevation models to map canopy height and AGB across ~7,000 ha of mangroves in the Marapanim estuary, northern Brazil. UAV-derived canopy height models reveal Avicennia stands reaching up to 53 m—the tallest recorded in Brazil—with mean plot-scale AGB of 648 Mg ha^{-1} and local maxima approaching 800 Mg ha^{-1}. Radar-derived DEMs systematically underestimate top-of-canopy height, with stronger biases observed in structurally heterogeneous forests. A DBH-based allometric approach combined with an empirical height–AGB model enabled calibrated wall-to-wall biomass mapping using UAV data. These results demonstrate that Amazonian mangroves rank among the tallest and most carbon-dense mangrove systems worldwide and highlight the importance of UAV-assisted calibration frameworks for improving satellite-based biomass and carbon estimates in complex coastal forest environments.

Keywords: Amazonian mangroves, Remote sensing, Above-ground biomass, Carbon Stock, Canopy height.

3.2 INTRODUCTION

Anthropogenic CO_2 emissions continue to increase due to fossil-fuel combustion and land-use change, reinforcing the urgency of identifying and protecting major terrestrial and coastal carbon sinks (Friedlingstein *et al.*, 2023; IPCC, 2023). Mangrove forests are globally recognized as highly efficient carbon-sequestering systems, storing large above- and below-ground carbon stocks and accumulating organic-rich sediments over long timescales (Alongi, 2022; Komiyama *et al.*, 2008; Rovai *et al.*, 2018). Despite occupying only ~13.6 M ha worldwide, mangroves provide disproportionate ecological, social, and economic benefits by stabilizing shorelines and buffering coasts against storms, tsunamis, floods, and hurricanes (Alongi, 2008, 2022; Cohen, Yao, *et al.*, 2024b; Menéndez *et al.*, 2020; Spalding *et al.*, 2021).

Mangrove structure—particularly canopy height—is a key predictor of above-ground biomass (AGB) and plays an important role in coastal protection efficiency (Das & Crépin, 2013; Meng *et al.*, 2021; Zaman *et al.*, 2023; Zhang *et al.*, 2012). While taller forests tend to exhibit higher AGB and above-ground carbon stocks (Trettin *et al.*, 2021), shorter mangroves can store substantial amounts of carbon in soils. When below-ground carbon is considered, total ecosystem carbon stocks in low-stature mangroves may equal or even exceed those of taller stands. Species such as *Rhizophora* and *Avicennia* exhibit particularly high sequestration potential (Donato *et al.*, 2011; Matos *et al.*, 2020; Simard *et al.*, 2019; Spivak *et al.*, 2019). Despite this global importance, the vertical structure and above-ground biomass (AGB) of mangroves remain incompletely characterized in several regions, particularly along the Amazon-influenced coast of northern Brazil, which hosts one of the largest and least disturbed mangrove provinces worldwide (Rovai *et al.*, 2022). Above-ground biomass (AGB) estimates in mangrove ecosystems show considerable spatial variability due to differences in forest structure, environmental conditions, and methodological approaches. Reported values range from approximately 315 Mg/ha for mature *Avicennia* stands in French Guiana (Fromard *et al.*, 1998) to 129.63 Mg/ha in the Colombian Pacific, associated with smaller trees (~30 m in height and mean DBH of 60.8 cm) (Yepes *et al.*, 2016). In contrast, large-stature mangroves have been documented with significantly higher values; for instance, Castellanos-Galindo *et al.* (2021) reported *Rhizophora* individuals reaching up to 57 m in height, with AGB estimates between 290.7 and 400.1 Mg/ha. At the regional scale, Rovai *et al.* (2022) reported an average of 205

Mg/ha for the state of Pará, in Brazil.

Radar-derived digital elevation models (DEMs), such as those from the Shuttle Radar Topography Mission (SRTM) and TanDEM-X, are widely used for large-scale mapping of vegetation height and biomass (Simard *et al.*, 2025). Nevertheless, their performance is strongly controlled by sensor wavelength, spatial resolution, and canopy architecture, often leading to systematic underestimation of top-of-canopy height in structurally complex forests (Rizzoli *et al.*, 2017; Simard *et al.*, 2006). In mangrove environments, where open canopies, tidal channels, mixed vegetation, and strong vertical heterogeneity are common, radar interferometric phase centers frequently occur below the true canopy apex, propagating errors into biomass and carbon stock estimates derived from EO products (Rizzoli *et al.*, 2017; Simard *et al.*, 2019; 2025).

Along the Amazon-influenced coast of northern Brazil, one of the largest and least disturbed mangrove provinces worldwide, structural metrics such as canopy height, crown architecture, and stand-level AGB remain poorly quantified (Rovai *et al.*, 2022). Existing information is largely derived from field studies with limited spatial coverage, which reported mature *Rhizophora* and *Avicennia* stands reaching approximately 20–30 m (Menezes *et al.*, 2008), leaving the true upper envelope of mangrove height and its implications for biomass and carbon storage unresolved. The known tendency of SRTM (~30 m) and TanDEM-X (~12 m) to smooth canopy structure further suggests that Amazonian mangroves may be systematically underrepresented in global carbon maps (Aslan and Aljahdali, 2022; Simard *et al.*, 2025).

Recent advances in unmanned aerial vehicle (UAV)–based photogrammetry now enable centimeter-scale reconstruction of forest structure, resolving emergent canopies, crown architecture, and individual trees that are often missed or smoothed by satellite sensors (Fatoyinbo *et al.*, 2018; Panagiotidis *et al.*, 2017). When used in combination with wall-to-wall satellite datasets, UAV observations provide a powerful means to calibrate and validate Earth observation products, diagnose sensor-dependent biases, and transfer field-based allometry to landscape and regional scales (Alvarez-Vanhard *et al.*, 2021; Silva *et al.*, 2018). Such multi-sensor data fusion approaches are increasingly recognized as essential for improving the retrieval of vegetation structure at complex, heterogeneous ecosystem scales (Naik *et al.*, 2021; Silva *et al.*, 2016; Wulder *et al.*, 2016).

Here, we develop and apply a transferable multi-sensor calibration framework that integrates ultra–high-resolution UAV photogrammetry with SRTM and TanDEM-X DEMs to quantify canopy height and AGB across 7,000 ha of mangroves along the Amazon-influenced coast of northern Brazil. Specifically, we (i) evaluate sensor-dependent biases in radar-derived canopy height retrievals, (ii) assess how forest structure and heterogeneity control these biases, and (iii) demonstrate how UAV-assisted calibration improves landscape-scale biomass mapping. By explicitly linking fine-scale structural observations to widely used EO products, this study provides methodological insights relevant not only to mangrove ecosystems, but also to the broader application of Earth observation in tall, structurally complex forested and coastal environments.

3.2.1 Study area

The northern Brazilian mangroves occur along 624,448 ha (Fig 3.1a), and the studied mangroves (7,931 ha) are located on the estuarine plains of the Marapanim River along the northeastern coast of Pará, Brazil (0°51′41.05″ S, 47°41′23.60″ W) (Fig. 3.1). This region experiences macrotidal conditions with semidiurnal tides ranging from approximately 3.5 m during neap tides to about 6 m during spring tides (Silva *et al.*, 2009). The area receives an average annual precipitation of around 2,300–2,800 mm, with a dry season from July to December and intense rainfall from January to April. The mean annual air temperature is approximately 27.3°C, and the relative humidity averages about 82% (Fitzjarrald *et al.*, 2008). Winds exhibit a clear seasonal pattern, with the windier season lasting from late July to early February, peaking in October at an average hourly speed of approximately 20 km/h. The calmer season runs from February to July, with the lowest levels in May, when wind speeds drop to around 14 km/h. However, Brazilian agencies have issued severe weather alerts for the Pará coast, with forecasted gusts reaching up to approximately 100 km/h in some events (Silva, 2024).

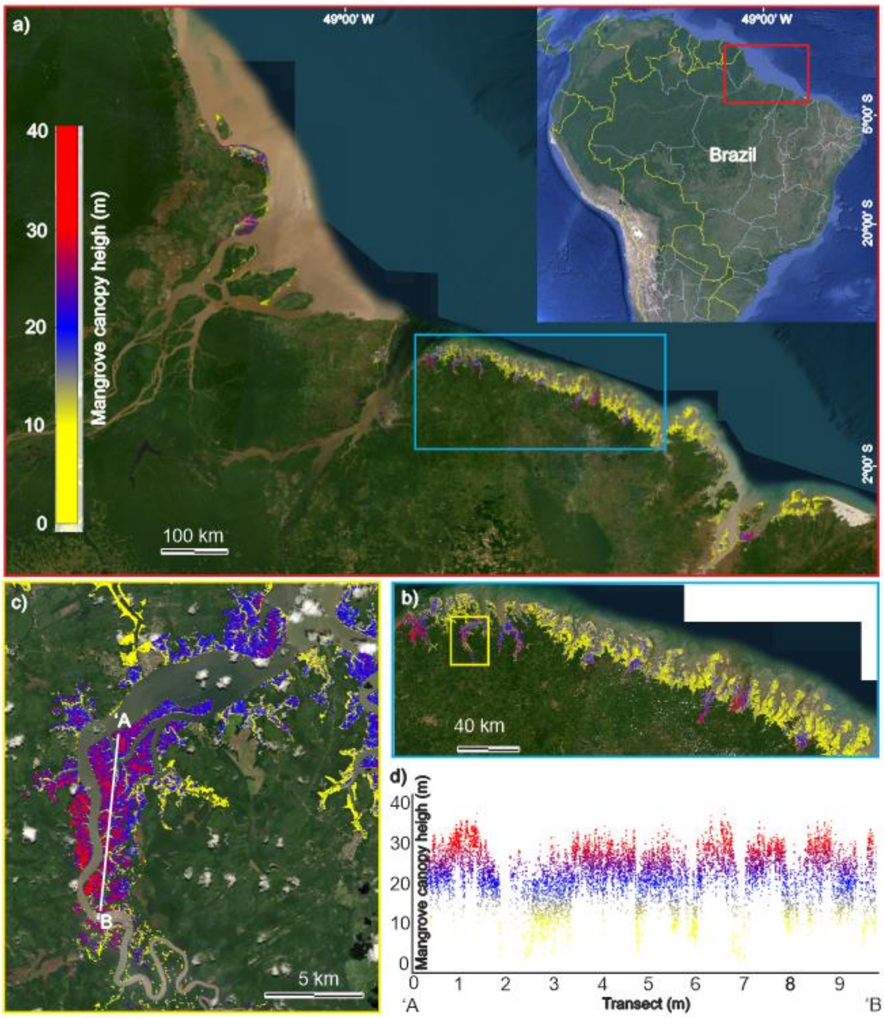

Figura 3.1 - a) Amazonian mangrove belt with its canopy height, b) mangrove distribution along the Para and Amapá states, c) mangrove canopy height along the Marapanim estuary, and d) transect based on TanDEM-X data.

3.3 MATERIALS AND METHODS

The use of unmanned aerial vehicles (UAVs) has become a reliable tool for estimating aboveground biomass and analyzing structural characteristics of arboreal vegetation (Castellanos-Galindo *et al.*, 2021; Navarro *et al.*, 2020; Panagiotidis *et al.*, 2017). This study employed geospatial analysis and ground-based validation conducted in the Amazonian mangroves to identify mangroves and their structure (tree height and DBH). This process enabled the application of allometric equations to estimate the above-ground biomass of mangroves. Our approach incorporated SRTM, satellite and drone data. Field measurements of topography were gathered using a Trimble Catalyst receiver with a differential Global Navigation Satellite System, supported by an electronic theodolite (model CST Berger DGT10). The overall methodology was structured in four stages (Fig. 2): (1) Regional analysis based on satellite, SRTM and TanDEM-X data; (2) Local-Scale Assessment based on field measurements and high-resolution drone datasets; (3) Data integration into statistical analysis; and (4) Generation of Above-Ground Biomass models for mangroves.

3.3.1 Regional analysis based on satellite, SRTM and TanDEM-X data

Multispectral QuickBird imagery (2.44 m; blue, green, and red bands) from Google Earth (Liang *et al.*, 2018) was used to delineate mangrove forests along the Marapanim estuary. Land cover was manually classified into six categories (mangrove, marsh, mudflat, sandy flat, water, and anthropogenic features) using Global Mapper following visual interpretation, which was preferred over automated methods due to spectral overlap and structural heterogeneity. *Avicennia* and *Rhizophora* trees were visually identified and manually digitized from satellite imagery using color-contrast (tone/texture) cues and their classification was verified through field observations (Fig. 3a). Regional elevation data from the Shuttle Radar Topography Mission (SRTM) and TerraSAR-X and Digital Elevation Model – X (TanDEM-X) were imported into Global Mapper in GeoTIFF format for processing. The SRTM dataset enabled the acquisition of surface heights derived from the phase difference of radar backscatter signals using radar interferometry. Despite the nominal absolute error (~16 m, LE90), prior studies have shown that when combined with ancillary topographic data, SRTM can estimate mean tree height with an error of only a few meters (Simard *et al.*, 2006). SRTM elevations are orthometric heights referenced to the EGM96 geoid, a global approximation of mean sea level. For mangroves, the ground surface lies near mean sea level (MSL), and mangroves are distributed between -2 and 3 m above mean sea-level in the study area. Thus, SRTM-derived elevations over mangroves can be used as a proxy for mean canopy height. For each digitized mangrove tree, canopy height was inferred from the SRTM Digital Elevation Model. In addition, we used 20 TanDEM-X Digital Elevation Model (DEM) GeoTIFF tiles downloaded from the NASA ORNL DAAC (Simard *et al.*, 2024). In mangrove regions, TanDEM-X data were acquired between December 2010 and April 2013, during the main acquisition phase of the global TanDEM-X mission, with a spatial resolution of 12 m and a vertical accuracy of 2.4 m (root-mean-square error, RMSE). The vertical reference system of the TanDEM-X DEM is based on the WGS84 ellipsoidal model. These elevation data were derived from the interferometric processing of bistatic X-band Synthetic Aperture Radar (SAR) pairs, performed by the German Aerospace Center (DLR) to generate the global TanDEM-X DEM, which was subsequently mosaicked and calibrated for canopy height estimation in mangrove regions. For the calculation of above-ground biomass (AGB) of mangroves, the "Apply Elevations to Selected Features" tool in Global Mapper Software version 26.1.2 was used to sample SRTM (7,000 ha) and

TanDEM-X (4,931 ha) elevation data of mangrove canopies. This difference in mangrove area results from the smaller mangrove extent identified in the TanDEM-X mangrove canopy height dataset, which delineates only areas where mangrove canopy height could be reliably retrieved. Because this omission resulted in an incomplete representation of the actual mangrove extent in the southern sector of the study area, we complemented the elevation data with the ESA Copernicus GLO-30 DEM (https://doi.org/10.5069/G9028PQB) for local analysis only. GLO-30 is a modified and updated version of the WorldDEM generated from TanDEM-X acquisitions and provides a globally available DEM at 30-m spatial resolution, distributed in 1° × 1° tiles. It uses geographic lat/lon coordinates (WGS84) and a vertical reference based on the Earth Gravitational Model 2008 (EGM2008), with absolute vertical accuracy <4 m. The integration of GLO-30 enabled us to map the full extent of mangroves in the southern sector and ensure consistent AGB calculations.

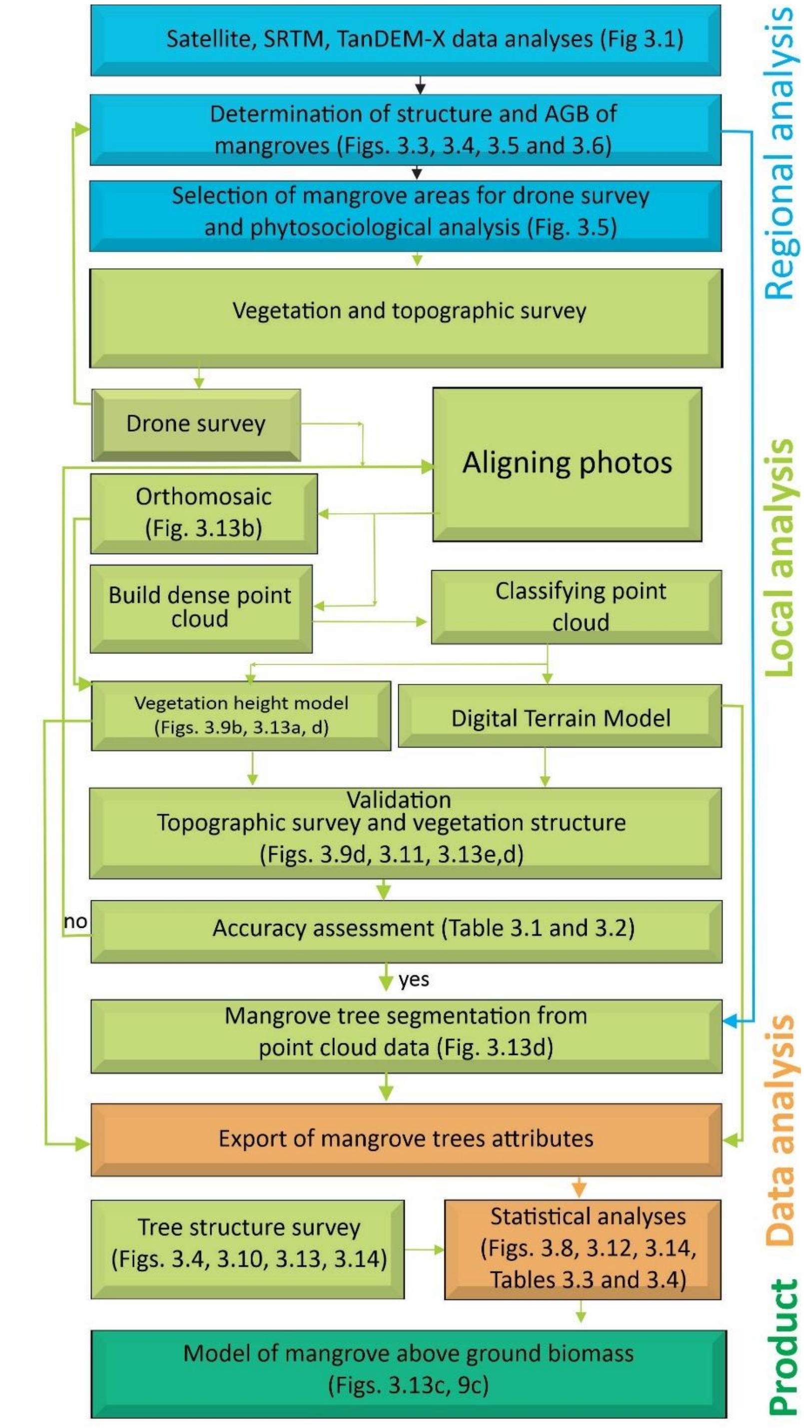

Figura 3.2. - Methodology flow.

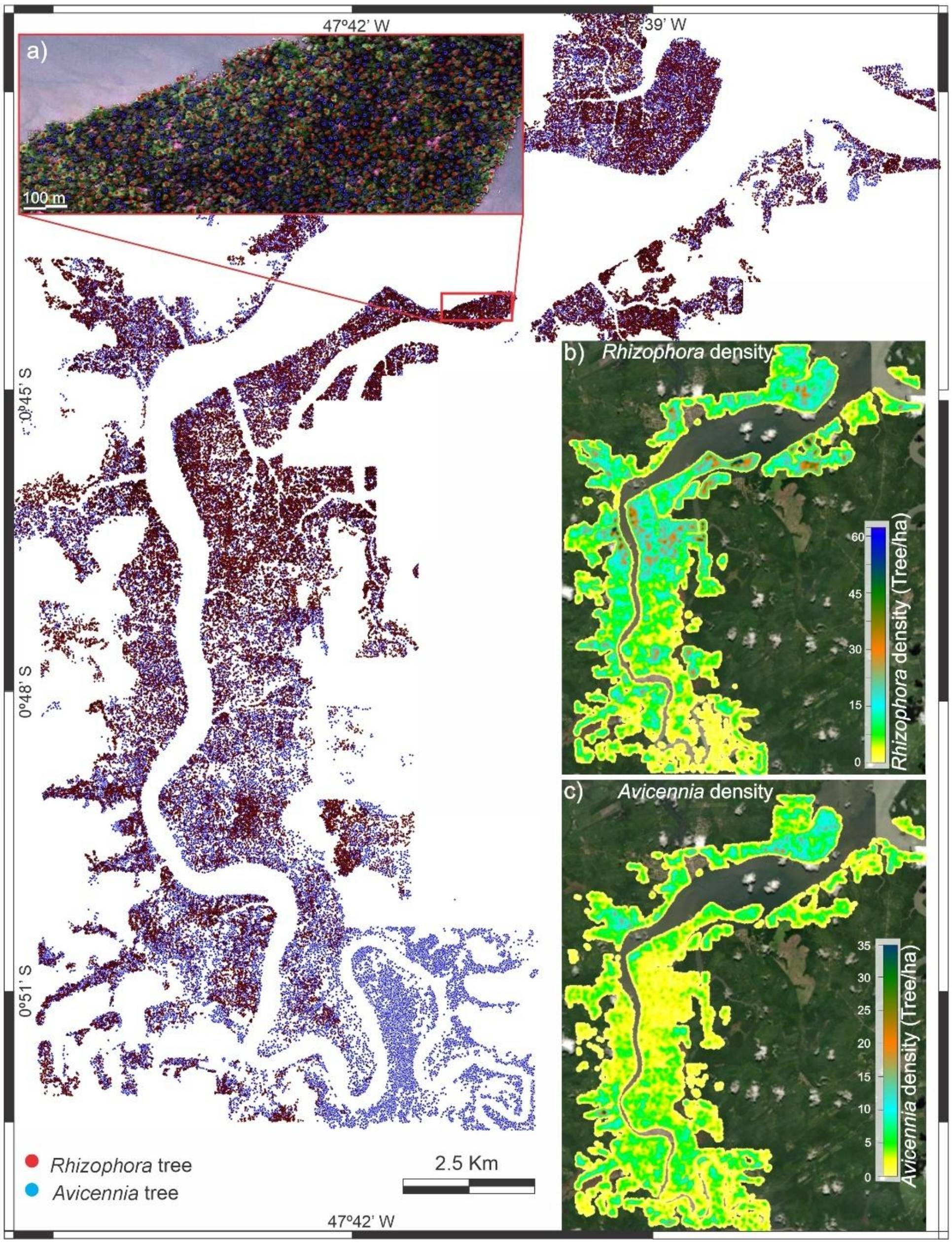

Figura 3.3- Distribution of Rhizophora and Avicennia trees in the study area, with: (a) satellite image highlighting the individualization of Avicennia and Rhizophora trees; (b) Rhizophora tree density; and (c) Avicennia tree density along the study area.

3.3.2 Drone-based local analysis

High-resolution images were acquired with a DJI Phantom 4 Advanced quadcopter equipped with GPS, inertial measurement systems, and an FC6310 RGB camera (4K/20 MP, 8.8 mm focal length, 12.8 mm sensor width, 5472 pixels). Mounted on a motion-compensated gimbal, the camera produced images with a ground sampling distance (GSD) of 2.6 cm/pixel at 100 m flight altitude, calculated as:

(1) $GSD = (Sw * H * 100/60) / (Fr * imH)$,

where *Sw* is sensor width (mm), *H* flight height (m), *Fr* focal length (mm), and *imH* image width (pixels) (PIX4D, 2013).

Drone surveys were planned in DJI Ground Station Pro with predefined waypoints (camera angle 90°, 90% forward overlap, 80% side overlap). Missions were flown in October 2024 and 2025, covering 912 ha. Each mission covered one mangrove area, with battery changes allowing ~48 ha per flight (17–20 min). In addition to nadiral drone flights, aerial photogrammetry of individual trees was conducted using circular flight missions around selected mangrove trees (Fig. 4). Flight plans were pre-programmed to maintain a constant altitude (10 – 60 m) and radius (20 – 40 m), ensuring complete coverage of the tree canopy and crown. The drone's camera was oriented at a 45° oblique angle to capture overlapping images from multiple perspectives, improving three-dimensional reconstruction and minimizing blind spots in the crown interior. The missions were executed with 85% overlap between images, providing sufficient redundancy for accurate structure-from-motion (SfM) photogrammetric processing and subsequent derivation of tree height and crown morphology.

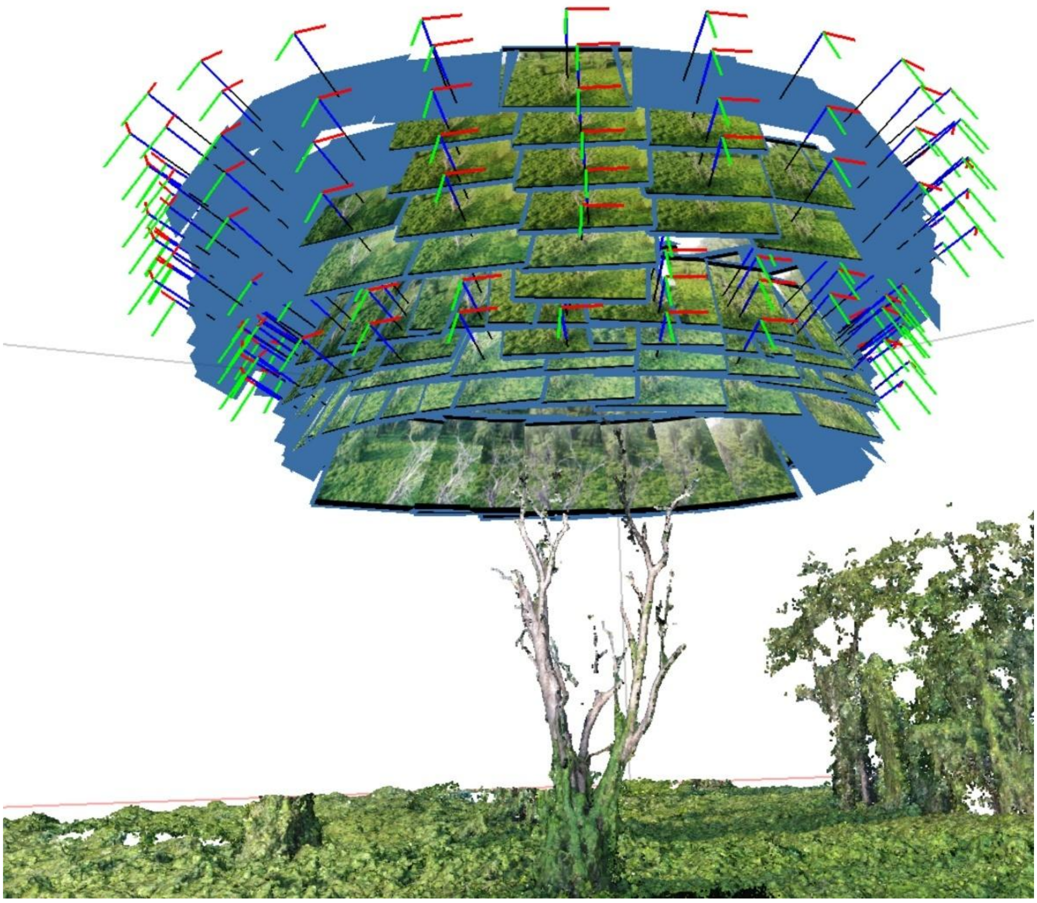

Figura 3.4- Point cloud in Agisoft Metashape showing a defoliated Avicennia tree, 32 m tall, selected as the target for a circular (orbit) drone flight. Colored points represent the reconstructed tree structure and its surroundings; the camera positions (blue squares) form a 360° ring around the tree. Orbit geometry maximizes side-looking coverage of the stem and major branches, enabling photogrammetric volume estimation of the trunk and limbs.

3.3.3 Ground control points (GCP)

Fieldwork was carried out in October 2024 and 2025 to collect planialtimetric data using a Trimble Catalyst antenna with Differential GNSS (sub-meter correction). After a 30-min stabilization, the base station accuracy was ±30 cm. Due to this delay, Catalyst measurements were used as reference points for a topographic survey with an electronic theodolite (CST Berger DGT10). Once the reference was established, the theodolite was used to determine relative elevations of Ground Control Points (GCPs). Planimetric accuracy was ±30 cm (Catalyst) and altimetric precision ±10 cm (theodolite). Ellipsoidal heights were converted to orthometric using the IBGE SIRGAS2000 geoid model. Twenty GCPs were obtained and applied to calibrate the DEM derived from photogrammetry. Mangrove tree heights were measured using a laser inclinometer. Four 100 × 100 m plots were surveyed to assess tree density, height, and diameter at breast height (DBH), providing ground validation for the photogrammetrically derived vegetation height model. The structural measurements obtained from these plots were used to characterize stand attributes and to support biomass estimation. All field data were compiled into a georeferenced dataset, which is archived as part of this study and is available upon request. In determining the mangrove area used for density estimation, only zones covered by mangrove vegetation were considered. However, open patches with fallen trees and areas showing regularly spaced mangrove trees interspersed with *Acrostichum*, Araceae, and Fabaceae species, as observed in the southern sector, were also classified as mangrove areas.

3.3.4 Field sampling and allometric AGB estimation.

Aboveground biomass (AGB) for *Rhizophora* and *Avicennia* was computed from field measurements of diameter at breast height (DBH) and tree height. We applied species-appropriate allometries that use DBH and wood density (ρ) only: (Komiyama *et al.*, 2005, 2008b) for *Rhizophora* and for *Avicennia* (Chave *et al.*, 2005). We did not find *Avicennia*-specific allometries validated for trees 30–50 m tall; therefore, we adopted the pantropical formulation of Chave *et al.* (2005), which is designed for a broad size range and commonly applied to tall tropical trees (≈10–60 m). After deriving AGB from DBH in the field dataset, we fitted height–AGB regressions (separately for *Avicennia* and *Rhizophora*) and selected the best-fitting model based on goodness-of-fit (e.g., R^2 and RMSE). These equations were then used to estimate per-tree AGB for the individuals delineated from satellite imagery using their extracted heights.

We selected 30 *Rhizophora* and 33 *Avicennia* trees in the northern and southern sectors of the study area for diameter at breast height (DBH, 1.3 m) and tree height (H) measurements. Tree height was measured in the field using a clinometer and georeferenced with a handheld GPS. These heights were then cross-checked against the canopy-height estimates derived from our Digital Elevation/Surface Models (DEM/DSM; CHM = DSM–DEM) at the individual-tree locations to confirm H. Above-ground biomass (AGB) for the sampled trees was estimated from DBH-only allometries that include wood density (ρ), using species-appropriate sources: for *Rhizophora* we applied the mangrove allometric model of Komiyama *et al.* (2008); for *Avicennia* we used the pantropical moist-forest model of Chave *et al.* (2005). In both cases, DBH is measured in centimeters (cm), ρ in grams per cubic centimeter (g cm^{-3}), and AGB in kilograms (kg).

- ***Rhizophora***

$$AGB = 0.251 \times \rho \times DBH^{2.46}$$

Equation 1. Aboveground biomass. Mangrove general model for Komiyama et al (2008)

- ***Avicennia***

$$AGB = \rho\, e^{-1.499+2.148\ln\, D+0.207(\ln\, D)^2-0.0281(\ln\, D)^3}$$

Equation 2. Aboveground biomass in moist-forest for Chave et al (2005). Where D = DBH

For each species, we used published wood density values (ρ = 0.9 and 0.74 g/cm^3, for *Rhizophora* and *Avicennia*, respectively) from Zanne *et al.* (2009). Individual-tree AGB from the sampled set was later used to (i) check consistency between field H and CHM-based H, and (ii) parameterize/validate the height-to-AGB transfer used in our wall-to-wall mapping. DBH was measured to the nearest 0.1 cm; heights were measured to the nearest 0.5–1 m, with outlier checks against CHM values (±2–3 m tolerance, re-measured in the field when exceeded). All coordinates are in the project UTM zone; GPS horizontal accuracy was typically ≤ 5–7 m under canopy breaks.

We selected the allometric equations based on the stature range for which each model was developed and validated, as well as the height range of our trees. For *Rhizophora*, we used the mangrove equation derived by Komiyama *et al.* (2008) because it was developed from mangrove taxa and encompasses the mid- to tall-canopy sizes observed at our site. For *Avicennia*, however, we found no species-specific allometric equation calibrated for very tall trees (≈30–50 m) comparable to those present in our study area. To avoid extrapolating beyond a model's support, we therefore adopted a generic pantropical equation (Chave *et al.*, 2005) that explicitly incorporates wood density and is documented to perform robustly across forest types and large size classes, including tall canopies. This choice prioritizes range compatibility and minimizes bias from extrapolating out of range.

3.3.5 3D Models generation and validation

Drone imagery (October/2024, October/2025) was processed in Agisoft Metashape Professional (2.2.0) using Structure-from-Motion (SfM) photogrammetry (Xu *et al.*, 2018) to generate orthomosaics, DSMs, and dense point clouds (3–5 cm spacing), constrained by Ground Control Points (GCPs) collected with a Trimble Catalyst DA2 and theodolite. Sparse point clouds were initially filtered using reprojection error, reconstruction uncertainty, image count, and projection accuracy, resulting in ~2 million reliable points over 912 hectares. Dense clouds (~15 million points) were subsequently produced and validated with 20 GCPs. Elevation and spectral data from 2,000 sample points were extracted using Global Mapper and statistically analyzed; classification based on RGB attributes and elevation separated *Avicennia* and *Rhizophora* stands from surrounding vegetation and geomorphological features. Classification outputs were compared with drone orthomosaics and validated with panoramic photos and field data. From the classified dense clouds, DTMs and DSMs were derived; canopy height was calculated by subtracting DTM from DSM, and DEMs were generated in Global Mapper using binning (10 points, ~2 cm spacing) with maximum-value filtering. Accuracy was evaluated by comparing DTM elevations with GCPs, yielding vertical errors <20 cm and within the ±30 cm tolerance of Catalyst data. Additionally, circular drone flights around individual trees generated dense 3D point clouds, capturing the geometry of the trunk and branches. These models, processed in MATLAB, enabled the volumetric estimation of woody components, allowing for the quantification of above-ground biomass at the individual-tree scale.

3.3.6 Mangrove trees segmentation

Individual *Avicennia* and *Rhizophora* trees were segmented from the classified point cloud. A high-resolution canopy height model (CHM) was generated to detect local maxima as seed points for segmentation, delineating crowns within mangrove stands previously classified as *Avicennia* or *Rhizophora*. Field data guided parameterization (tree spread 10–50 m; minimum height 5 m; medium threshold 20 m; high threshold 52 m). For each crown cluster, tree height was estimated as the difference between the highest point and DTM elevation. The "Create Density Grid" tool generated a raster of tree density. Automated outputs were validated against manual counts in UAV orthomosaics (Table 3.1).

3.3.7 Orthomosaic classification

High-resolution RGB orthomosaics were generated in Agisoft Metashape and orthorectified using DEM data and the inertial motion sensor. To identify mangrove trees, we applied a false-color composite of the red, green, and blue bands, which enhanced the spectral contrast between the tree crowns and surrounding features. Vegetation indices derived from the RGB dataset, including the Visible Atmospherically Resistant Index (VARI) and the Excess Green Index (ExG), facilitated the separation of mangrove trees from adjacent vegetation, mudflats, sandy barriers, and anthropogenic features in Global Mapper v.26.1.2. Training and validation were supported by field observations, panoramic aerial photographs, and 20 ground control points (GCPs), ensuring radiometric calibration and accurate spatial alignment of the orthomosaics.

3.3.8 Data integration and analysis

A comparative statistical analysis was performed to assess the consistency between field and drone-derived measurements of elevation, tree height, and aboveground biomass (AGB). Linear regressions were applied to each variable, and model fit was evaluated using the coefficient of determination (R^2) as the primary metric. Model accuracy was also quantified using three error metrics: bias (BIAS), mean absolute error (MAE), and root mean square error (RMSE), calculated using the following equations:

$$BIAS = \frac{1}{n} * \sum_{i=1}^{n} (x_i - y_i)$$

Equation 3. BIAS of the model accuracy.

$$MAE = \frac{1}{n} * \sum_{i=1}^{n} |(x_i - y_i)|$$

Equation 4. Mean absolute error.

$$RMSE = \sqrt{\frac{1}{n} * \sum_{i=1}^{n} (x_i - y_i)^2}$$

Equation 5. Root mean square error.

Where x_i represents the values obtained by SRTM and Tandem-X measurements, and y_i represents the values obtained directly from field/UAV measurements of the trees.

3.3.9 Above-Ground Biomass

In this study, aboveground biomass (AGB) was estimated from field-measured DBH using species-appropriate allometric models that incorporate wood density. For *Avicennia*, we applied the pantropical equation of Chave *et al.* (2005), as no species-specific models are available for large individuals (30–50 m) in our study region. In contrast, AGB for *Rhizophora* was derived using the mangrove-specific model of Komiyama *et al.* (2008), which has been widely validated for this genus under intertidal conditions.

Based on the field-derived AGB values, we then fitted an empirical relationship between AGB and tree height using canopy height estimates obtained from the field–UAS workflow. This regression enabled the spatial extrapolation of biomass across the study area using high-resolution drone-derived canopy height products, while preserving the consistency of field-based allometric estimates

3.4 RESULTS

3.4.1 Regional analysis

Satellite images enable us to identify 7,000 ha of mangroves along the Marapanim Estuary River, distributed between -2 and 3 m above mean sea level. Terra Firme vegetation, which is an upland forest that is never flooded by tidal waters, occurs >3 m above the mean sea-level. It was identified that 114,428 and 159,732 trees of *Avicennia* and *Rhizophora* had heights of up to 51 and 39 meters, with densities of up to 87 and 100 trees ha^{-1}, respectively, ($\bar{x}$ = 39 trees ha^{-1}). Based on SRTM data, 70% of *Avicennia* trees are between 15–25 m in height (3-35 trees ha^{-1}), while 75% of *Rhizophora* trees fall within the same range (3-60 trees ha^{-1}) (Figs. 3.1 and 3.4). The mangrove AGB in this area was ~70 Ton ha^{-1} (Fig. 3.5). Considering the TanDEM-X data, our study area has 69,288 *Avicennia* (1 – 40 m tall) and 123,352 *Rhizophora* (1 – 39 m tall) trees distributed over 4,900 ha, revealing a mangrove AGB of 136 Ton ha^{-1} (Fig. 3.6). The histogram derived from the SRTM data showed that the canopy height distributions for *Avicennia* and *Rhizophora* were centered at approximately 20 m and 21 m, respectively, indicating a similar canopy structure for both genera when observed by this sensor. In contrast, the TanDEM-X data revealed a systematic shift toward higher classes, with both genera showing height distributions centered around 25 m (Fig. 3.4). The comparison between TanDEM-X and SRTM canopy height models revealed a consistent trend of higher mangrove height estimates in the TanDEM-X data across 80% of the study area. Specifically, approximately 70% of the mangrove stands exhibited a positive height difference ranging from 0 to 5 m, while an additional 10% showed differences between 5 and 7.5 m in favor of the TanDEM-X model. Fewer mangrove canopy heights were inferred from the TanDEM-X data in the southern part of the study area, and these were consistently lower than those derived from the SRTM data (Fig. 3.7). We detected a decrease in AGB, in (i) the northern sector (60 Ton ha⁻¹ and 104 Ton ha⁻¹ by SRTM and TanDEM-X, respectively), where mixed *Avicennia–Rhizophora* stands occur, and an increase in (ii) the southern sector (101 Ton ha⁻¹, by SRTM), characterized by monospecific *Avicennia* mangroves. To verify these patterns, we selected representative sites for *in situ* validation, including UAS (drone) surveys and ground measurements of canopy height and diameter at breast height (DBH).

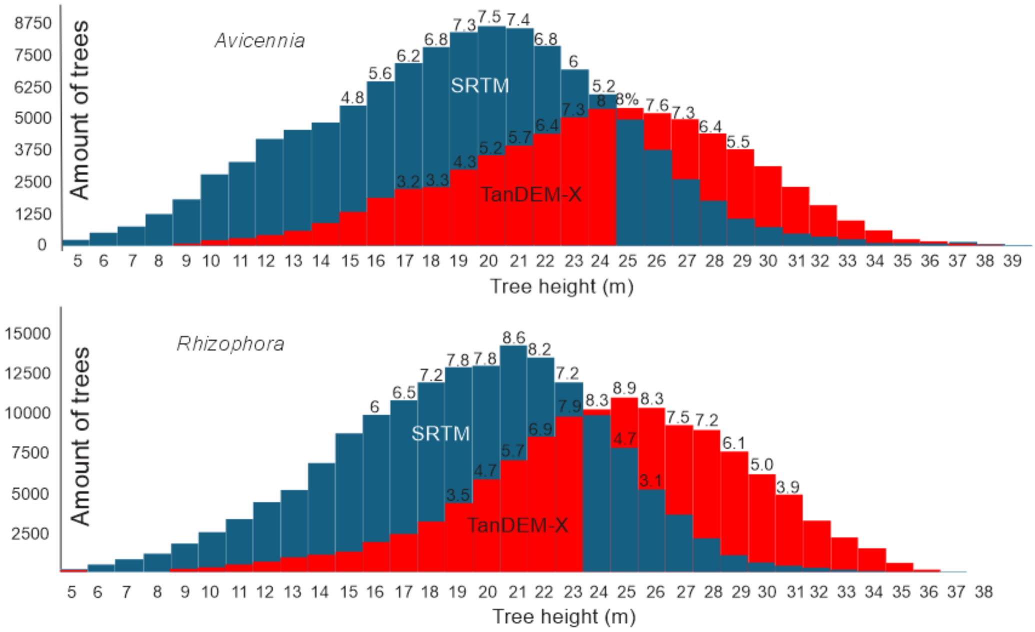

Figura 3.5. - Histograms showing the relationship between tree abundance and canopy height of Avicennia and Rhizophora in the study area, based on SRTM and TanDEM-X data.

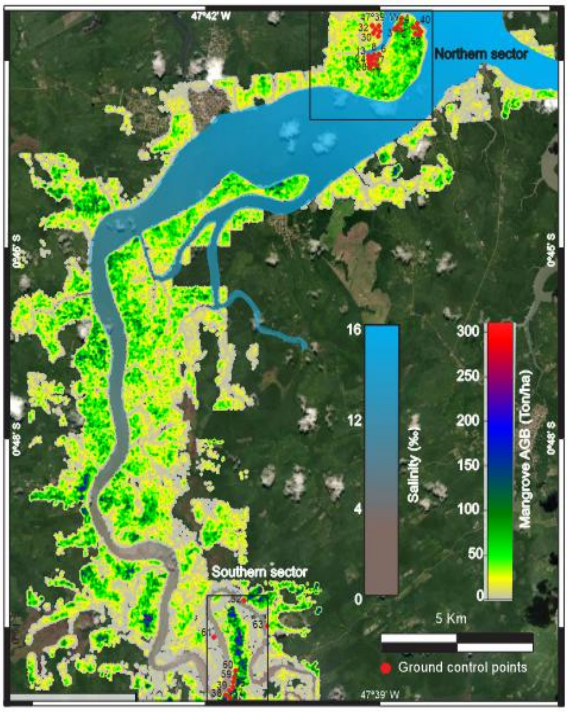

Figura 3.6- Above-ground biomass of studied mangroves based on SRTM mangrove canopy height with water salinity along the Marapanim River during the summer. Red points indicate ground control points for the mangrove canopy height (see Table 1 and 2).

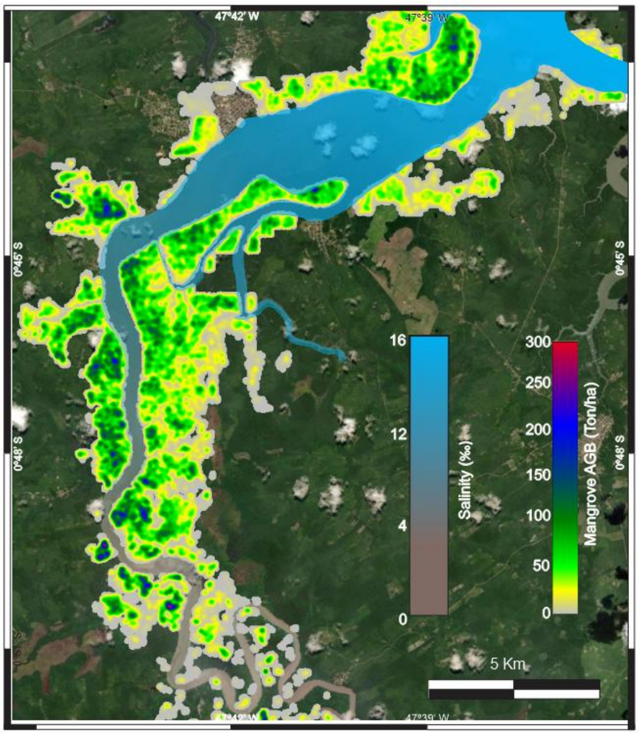

Figura 3.7- Above-ground biomass of studied mangroves based on TanDEM-X mangrove canopy height with water salinity along the Marapanim River during the summer.

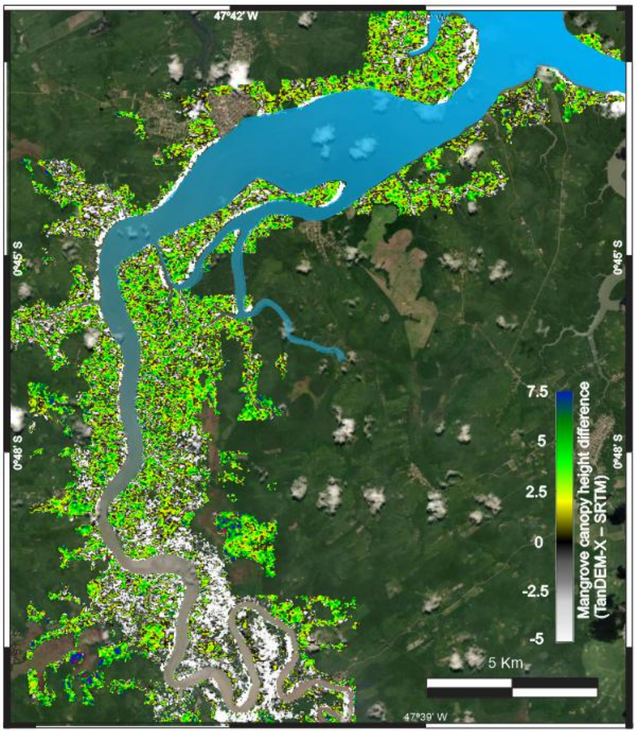

Figura 3.8- Difference in mangrove canopy height derived from SRTM and TanDEM-X datasets. The map shows spatial variations in canopy height differences across the study area, oscillating ±5 m. Positive values, indicating higher TanDEM-X values, are observed in the central and northern portions of the study area. In contrast, the southern sector exhibits lower mangrove canopy height detected by TanDEM-X relative to SRTM data.

3.5 LOCAL ANALYSIS

3.5.1 Southern sector

Based on drone photogrammetry, the mangrove stand covers 48.95 ha and comprises 2,518 mapped *Avicennia* trees (51 trees ha^{-1}). According to the histogram, the distribution of *Avicennia* trees, in terms of both number (y-axis) and height (x-axis), is unimodal, with canopy heights ranging from 5 to 53 m. There is a clear predominance (53%) in the 26–40 m class, followed by 12–26 m (36%). Fewer trees occur at both extremes, with smaller classes including 5–12 m (5%) and 40–53 m (5%) (Fig. 3.8 and 3.9b). Drone-derived photogrammetry enabled us to clearly distinguish nine emergent *Avicennia* trees, ranging in height from 45 to 53 m (Fig. 3.9d). However, the SRTM-derived data indicated a predominance of *Avicennia* trees with heights between 10 and 22 m (~84% of the total), followed by a secondary group (8%) composed of trees ranging from 6 to 10 m, resulting in an estimated above-ground biomass of 101 Mg ha^{-1}. The TanDEM-X data showed that 77% of *Avicennia* trees were concentrated in the 6–14 m height range, corresponding to a considerably lower above-ground biomass of 30 Mg ha^{-1} (Fig. 3.8). Field inspections and UAV imagery revealed that mangroves are dominated by mature, tall *Avicennia* (26 – 40 m), with relatively few juveniles/saplings and few exceptional giants (>40 m). In addition, widespread crown breakage/apical damage was recorded, particularly among the largest trees (>20 m) and with DBH ≥ 1 m. Additionally, some trees ≥ 25 m were completely defoliated, suggesting they were standing dead (Fig. 3.10). Tall trees showed heavy infestation by climbing vegetation along the trunk (Fig. 3.11b), while smaller trees (height < 20 m; DBH ≤ 1 m) exhibited clean boles (no climbing vegetation, Fig. 3.11e) and no evidence of structural damage. The estimated aboveground biomass (AGB) averages 648 Mg ha^{-1} across the stand, with hotspots approaching ~800 Mg ha^{-1} in the tallest mangrove spots (Fig. 3.9c).

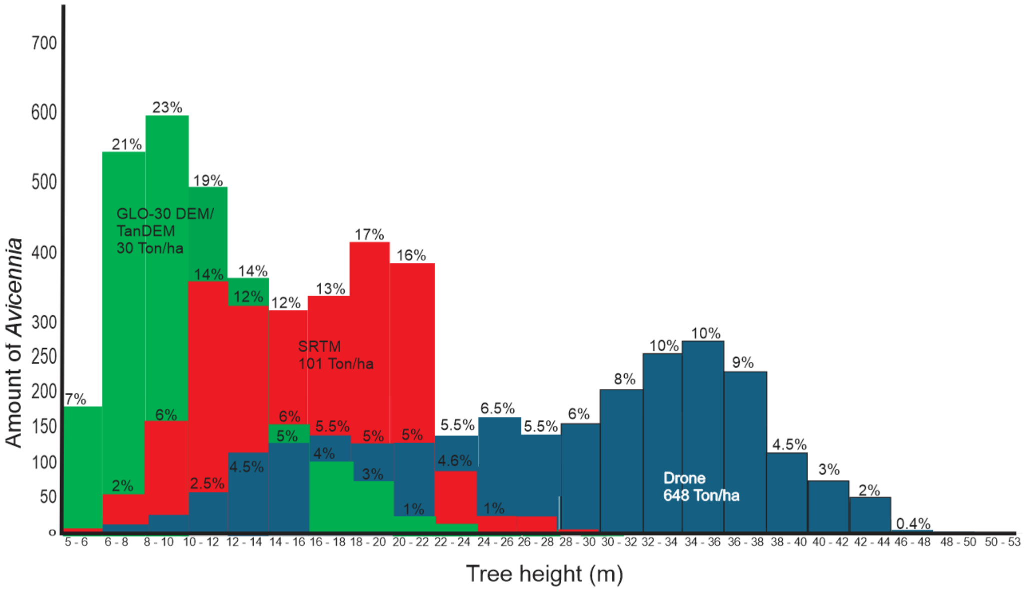

Figura 3.9.- Integrated histograms showing the relationship between the number of Avicennia trees (y-axis) and tree height (x-axis), derived from three different canopy height datasets: GLO-30 DEM/TanDEM-X (30 Mg ha^{-1}), SRTM (101 Mg ha^{-1}), and UAV (648 Mg ha^{-1}). A total of approximately 2,500 Avicennia trees were analyzed to estimate their heights and the distribution of above-ground biomass across the southern study area.

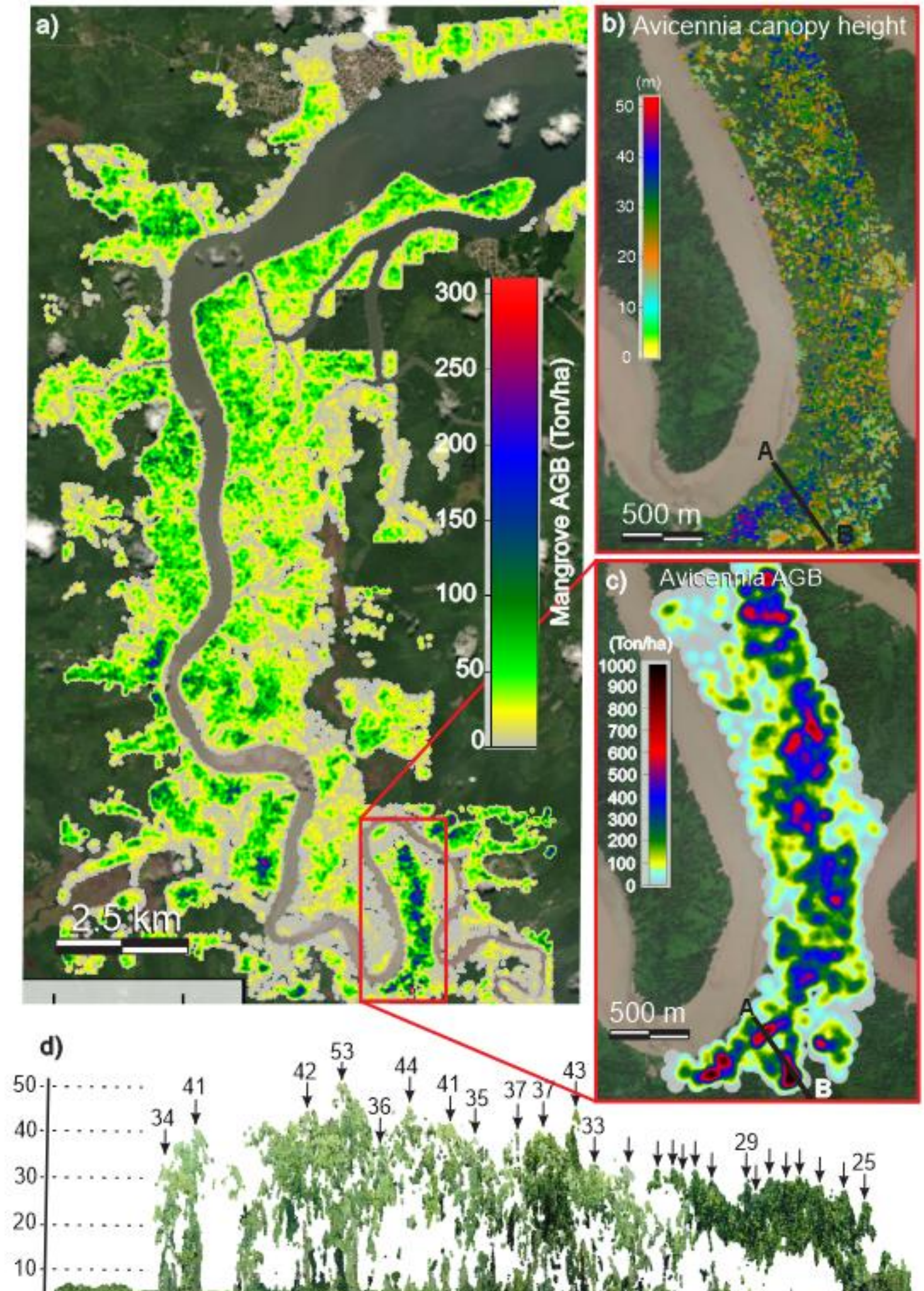

Figura 3.10. - (a) Map of above-ground biomass (Mg ha⁻¹) across the study area derived from SRTM data; (b) *Avicennia* trees in the southern sector showing their canopy height (m); (c) above-ground biomass of *Avicennia* estimated from UAV photogrammetry; and (d) transect profile highlighting the tallest *Avicennia* trees within the study area.

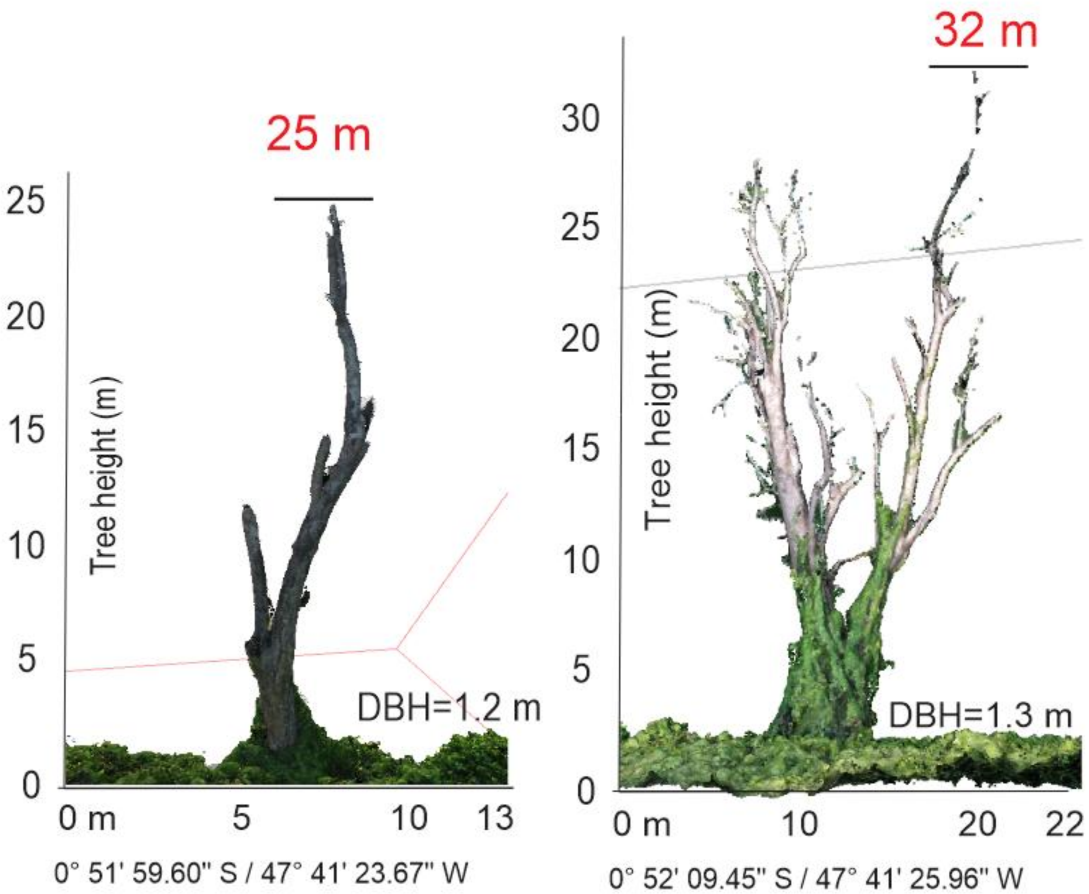

Figura 3.11- Detailed photogrammetric product derived from UAV imagery showing completely defoliated Avicennia trees, with individual tree height and diameter at breast height (DBH) measurements extracted from the 3D point cloud and in situ measures.

Figura 3.12- Field photographs showing: (a) mangrove stand with sparsely distributed Rhizophora roots; (b) *Avicennia germinans* trunk with a diameter at breast height (DBH) of 1.5 m, infested by climbing vines; (c) mangrove forest densely dominated by Rhizophora; (d) isolated mangrove; (e) *Rhizophora* trunk with a diameter at breast height (DBH); (f) mangroves along the Marapanim River.

3.5.2 Northern sector

In the northern sector of the study area (745 ha), UAV-based photogrammetry enabled the identification of 57,718 *Avicennia* and 24,850 *Rhizophora* trees, the estimation of their canopy heights, and the development of detailed canopy height histograms for both *Rhizophora* and *Avicennia* stands (Figs. 3.13a and 3.12). Approximately 60% of *Rhizophora* trees exhibited heights between 19 and 27 m, while 14% reached between 27 and 34 m. For *Avicennia*, 56% of individuals ranged from 21 to 29 m in height, and 6% were between 29 and 34 m. The mean tree density was 110 trees ha^{-1} (Fig. 3.13d), confirmed through canopy segmentation of each tree (120 trees ha ^{1}) based on the point cloud and by counting the trees within this 1-ha plot (Fig. 3.13d). These data indicated an above-ground biomass (AGB) of 430 Mg ha^{-1} (Fig. 3.13c). The SRTM-derived model revealed comparatively lower canopy estimates, with 65% of *Rhizophora* stands ranging from 17 to 23 m, and 69% of *Avicennia* within the same height interval. The corresponding AGB derived from SRTM data was 201 Mg ha^{-1}. In contrast, TanDEM-X data showed a slightly improved vertical structure representation, with 65% of *Rhizophora* between 17 and 25 m and 70% of *Avicennia* between 19 and 27 m, resulting in an estimated AGB of 220 Mg ha^{-1}.

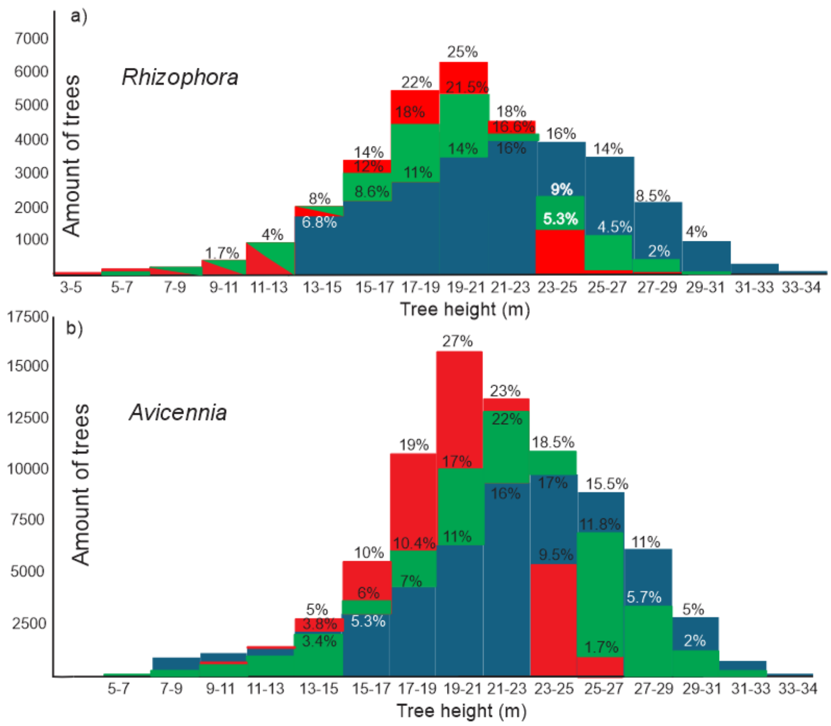

Figura 3.13- Integrated histograms showing the relationship between the number of a) Rhizophora and b) Avicennia trees (y-axis) and tree height (x-axis), derived from three different canopy height datasets: SRTM in red color (201 Mg ha^{-1}), TanDEM-X in green color (220 Mg ha^{-1}), and UAV in blue color (430 Mg ha^{-1}). A total of approximately 49,700 Rhizophora and 115430 Avicennia trees were analyzed to estimate height and corresponding above-ground biomass distribution across the northern study area.

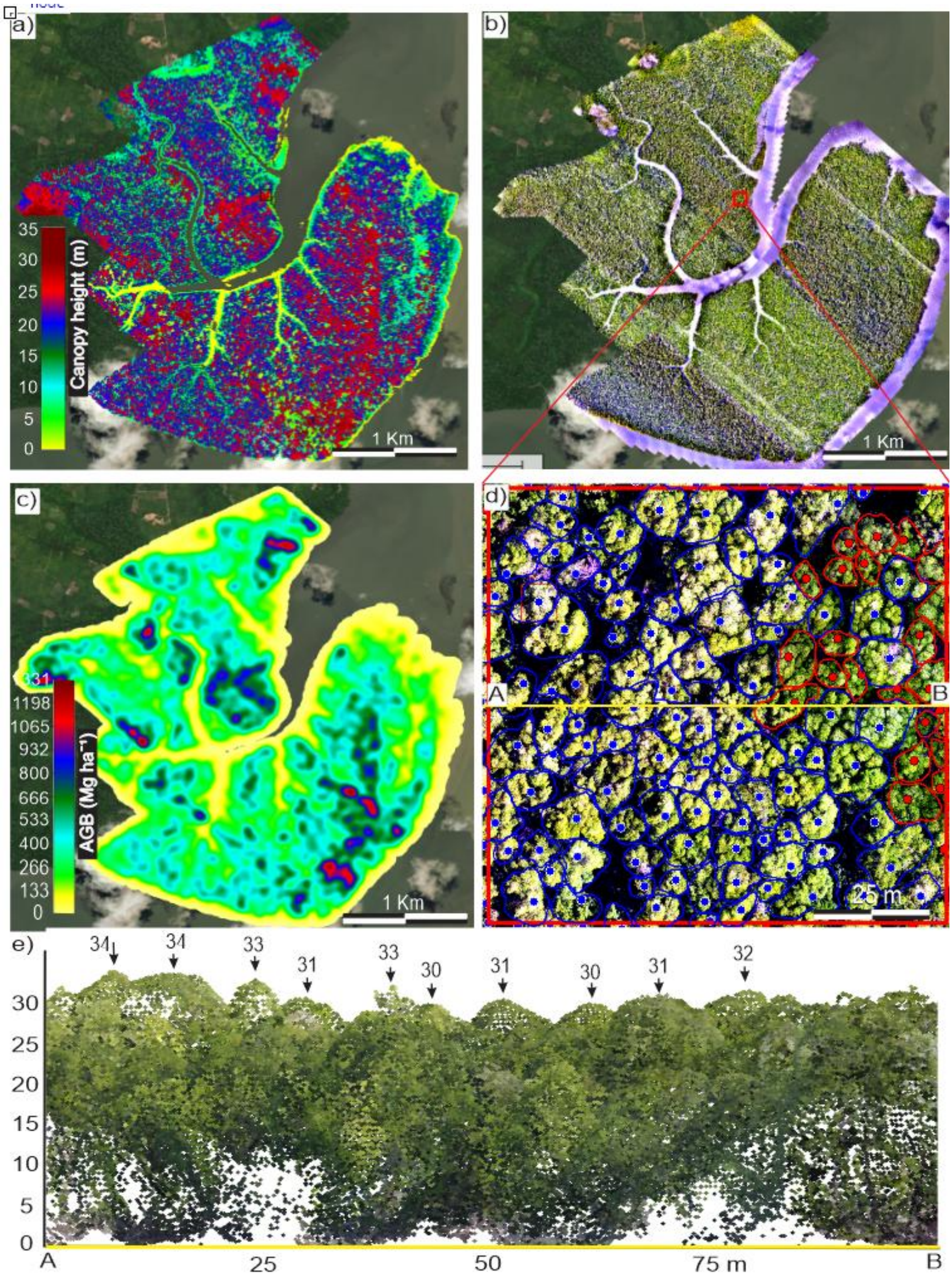

Figura 3.14- Northern sector with (a) mangrove canopy height model derived from UAV data; (b) orthomosaic with 2-cm spatial resolution; (c) distribution of AGB of mangrove;
(d) one of the five 1-ha plots selected for field measurements of tree height, DBH, mangrove type, and stand density, including crown segmentation of individual trees;
(e) A–B transect across the study area highlighting tree height variation (m).

3.6 DISCUSSION

The three key parameters controlling mangrove AGB estimation are (1) canopy area, (2) tree density by genus, and (3) the choice of allometric equations. Their combined influence determines the accuracy of biomass assessments, and each is evaluated below.

3.6.1 Mangrove area

The areas considered for AGB quantification using SRTM and TanDEM-X differed because the TanDEM-X mangrove-specific dataset delineated a smaller mangrove extent than the area mapped through our UAV- and satellite-based classification (Figs. 3.6 and 3.7). While our classification identified the full 7,000-ha mangrove domain—including both dense and structurally heterogeneous stands—the TanDEM-X dataset mapped mangroves more conservatively (4,900 ha), excluding mangrove zones with mixed vegetation, or transitional mangrove forest–herbaceous/ferns boundaries. This issue was particularly pronounced in the southern sector of the study area, where the TanDEM-X mangrove-specific dataset identified only a limited number of mangrove patches, probably due to low interferometric coherence in stands dominated by tall, sparsely spaced *Avicennia* trees interspersed with herbaceous, ferns, and shrub vegetation. Because this omission resulted in an incomplete representation of the mangrove canopy height extent, we complemented the elevation data with the ESA Copernicus GLO-30 DEM. The full extent of the mangrove area in the southern sector was delineated from high-resolution UAV imagery, and integrating GLO-30 enabled us to fill gaps left by TanDEM-X and ensure AGB calculations. The incorporation of ESA Copernicus GLO-30 DEM data was limited exclusively to the local analysis of the southern study sector (48.95 ha), where TanDEM-X coverage was virtually absent. In this area, GLO-30 was used to generate local estimates of canopy height and AGB from elevation data. In the full extent analysis of the 7,000-ha study area and the northern study area (745 ha), however, TanDEM-X data (vertical accuracy ~2 m) were not mixed with GLO-30 data (vertical accuracy ~4 m). All regional-scale assessments relied strictly on TanDEM-X to ensure consistency in resolution and vertical accuracy across the entire dataset.

The delineation of mangrove extent was restricted to areas where a continuous or semi-continuous mangrove canopy was identified. However, zones containing canopy gaps or sparse tree cover were inevitably included within the classified mangrove polygons. Consequently, these heterogeneous areas may dilute both the estimated tree density and the calculated AGB, since regions with reduced canopy occupancy contribute proportionally less biomass while still being mapped as mangrove. This dilution effect becomes more pronounced as the spatial resolution of the imagery decreases—particularly when using satellite-based datasets—because lower-resolution pixels tend to aggregate gaps and vegetated patches into a single mangrove class, further smoothing structural variability and underrepresenting true stand density. These differences highlight how sensor characteristics and coherence thresholds can influence mangrove extent detection and underscore the importance of using high-resolution UAV and optical data to refine radar-derived biomass estimates.

3.6.2 Tree Density

Accurate estimates of mangrove AGB require separating tree density by genus, particularly for *Rhizophora* and *Avicennia*, because these groups differ markedly in structural architecture and biomass allocation. Even when trees from both genera reach similar heights, *Avicennia* typically exhibits substantially higher biomass due to its thicker trunks compared to *Rhizophora*, a pattern widely documented in mangrove allometric studies (Komiyama *et al.*, 2008a; Menezes *et al.*, 2008). As a result, treating mangrove stands as compositionally uniform can introduce significant errors in biomass estimation. Therefore, stand density must be quantified independently for each genus to ensure the appropriate application of allometric models and the production of accurate AGB estimates. A few *Laguncularia racemosa* individuals occur within the study area and exhibit spectral characteristics similar to *Avicennia Germinans* in both UAV and satellite imagery. These trees were therefore interpreted as *Avicennia* for AGB estimation, as their canopy structure and trunk morphology closely resemble those of *Avicennia*. Given their comparable form and structural contribution at the plot scale, treating these *Laguncularia* individuals as *Avicennia* introduces minimal bias into the biomass calculations. Regional satellite data (QuickBird, 2.4 m) indicated moderate densities (mean 39 trees ha^{-1}, Fig. 3), whereas at the local scale, UAV photogrammetry (3 cm GSD) revealed substantially higher tree densities and more detailed structural patterns in the southern sector (~50 trees ha^{-1}) with a regular spacing pattern between 10 and 20 m. The northern sector presented a more closely spaced (6–13 m), resulting in a higher density (~110 trees ha^{-1}). These higher tree densities derived from photogrammetry reflect the finer spatial resolution of UAV imagery (~3 cm) compared to satellite imagery (2.4 m). The canopy segmentation process incorporated a high-resolution DEM, enabling precise delineation of individual crowns (Fig. 14e). Field surveys confirmed the UAV-based estimates (Fig. 3.14d).

3.6.3 Allometric equations

From the perspective of the allometric equation employed, we estimated AGB for *Avicennia* using a generic pantropical equation (Chave *et al.*, 2005), with field-measured DBH as the predictor (Table 1), because no *Avicennia*-specific allometric model exists for very tall trees (30–50 m). This choice is consistent with best practice when species-specific models are unavailable, as DBH-based pantropical equations have been shown to perform robustly across forest types (Chave *et al.*, 2005). We note that DBH generally explains more variance in AGB than height for mangroves, a result echoed in recent allometric syntheses, which report DBH as the most robust single-predictor correlate of mass (e.g., Price *et al.*, 2024, 2025). To map biomass wall-to-wall, we then transferred the DBH-based plot AGB to remote sensing by fitting an empirical AGB–height function (exponential, Fig. 3.15): plot AGB (y) versus tree height (x), and applying that relationship to tree-height estimates derived from our Digital Elevation/Surface Models (SRTM, TanDEM-X and UAV data). This two-step "DBH→height→AGB" strategy is commonly used in biomass mapping when DBH is only available at plots, while height is a reliably retrievable structural metric from remote sensing (Wang *et al.*, 2019). Although height alone is typically a weaker direct predictor of mangrove AGB than DBH, the transfer is justified operationally because height can be mapped consistently at scale, while DBH cannot (Lucas *et al.*, 2020). Finally, where available, species-specific mangrove allometry (*Rhizophora*) should be used in preference to generic forms. Our treatment of *Rhizophora,* based on field-measured DBH (Table 3.2), follows this principle (Komiyama *et al.*, 2008).

To evaluate the degree of reliability of the allometric equation used to estimate *Avicennia* AGB from tree height, which was derived from a generic allometric equation, we conducted circular drone flights (concentric "orbit" missions) around individual *Avicennia* trees and used close-range photogrammetry to reconstruct 3D models of the stems and major branches (Figs. 16 and 17). From these models, we estimated woody volume and converted it to mass using the published wood density of *Avicennia* (0.74 g/cm^3). Despite the relatively high correlation ($R^2 = 0.77$) between *Avicennia* AGB and tree height, indicating that height is a reasonable proxy for biomass, the AGB derived from photogrammetry of individual *Avicennia* tree were consistently lower than the AGB predicted by the generic allometric equation based on field-measured DBH for the same trees (Fig. 3.15). This divergence suggests a systematic positive bias in the allometric estimates for *Avicennia* in our study area. This discrepancy may be attributed to occlusion: many secondary and fine branches were not reconstructed because they were obscured by foliage in the images, and therefore their total volume was not captured by the photogrammetric models of individual *Avicennia* trees (Figs. 3.16 and 3.17). To minimize this effect, we also mapped defoliated trees (Fig. 3.11); however, the photogrammetry-based masses remained significantly lower, most likely because numerous small branches had already been lost. Then, photogrammetric estimates (concentric “orbit” missions) tend to plot marginally below the exponential allometric curve (Fig. 3.15), indicating a slight underestimation of biomass relative to the model prediction (AGB, Tree height, $y=0,0055x^{4.3071}$, $R^2=0.77$). Therefore, the *Avicennia* biomass values derived from the allometric curve should be treated as “at least” estimates—i.e., minimum benchmarks rather than exact totals.

Tabela 3.1- Geographic coordinates (latitude, longitude), tree height (m), diameter at breast height (DBH, cm) and above-ground biomass (AGB) for each sampled *Avicennia* individual. AGB values were calculated using the allometric equations of Chave *et al.* (2005).

GCP	LAT/LONG	HEIGHT UAV (M)	DBH (CM)	BIOMASS (KG) (CHAVE *ET AL.*, 2005)	HEIGHT (SRTM)	HEIGHT (TANDEM)
18	0°41'48.4089" S, 47° 38' 49.2099" W	21	60	5094	20	21
19	0° 41' 51.3648" S, 47° 38' 57.7117" W	21	50	3256	14	17
24	0° 41' 51.9502" S, 47° 38' 58.1322" W	20	47	2792	18	17
27	0° 41' 51.8859" S, 47° 38' 56.8394" W	39	122	26390	20	17
35	0° 52' 14.5337" S, 47° 41' 29.8815" W	40	130	30306	28	34
36	0° 52' 14.7287" S, 47° 41' 30.0755" W	49	173	55313	30	26
37	0° 52' 15.3466" S, 47° 41' 30.4961" W	23	76	8975	22	23
38	0° 52' 15.2799" S, 47° 41' 32.6939" W	32	94	14712	28	29
39	0° 52' 15.8663" S, 47° 41' 31.6277" W	50	170	53368	31	34
40	0° 41' 22.7695" S, 47° 38' 04.2986" W	15	12	80	14	8
41	0° 41' 21.2568" S, 47° 38' 06.9601" W	13	10	49	12	13
42	0° 41' 24.4698" S, 47° 38' 06.7060" W	12	15	145	10	7
43	0° 41' 23.3948" S, 47° 38' 02.1084" W	11	15	145	10	8
44	0° 41' 23.7707" S, 47° 38' 07.5055" W	10	15	145	10	10
45	0° 41' 16.9980" S, 47° 38' 11.5692" W	20	60	5094	18	20
46	0° 41' 18.8012" S, 47° 38' 09.5546" W	10	20	310	9	10
47	0° 41' 20.0231" S, 47° 38' 08.5344" W	10	22	398	9	11
48	0° 41' 22.6486" S, 47° 38' 09.8952" W	12	17	201	10	13
49	0° 41' 24.3496" S, 47° 38' 11.0828" W	16	18	234	15	15
50	0° 41' 25.0724" S, 47° 38' 10.5288" W	12	17	201	10	12
51	0° 41' 13.5888" S, 47° 38' 15.3186" W	10	16	172	9	11
52	0° 41' 12.7986" S, 47° 38' 16.6996" W	15	20	310	13	15
53	0° 52' 09.6150" S, 47° 41' 24.5440" W	30	120	25450	28	27
54	0° 52' 14.2208" S, 47° 41' 33.2930" W	26	120	25450	25	26
55	0° 52' 14.7583" S, 47° 41' 28.7459" W	40	170	53368	31	34
56	0° 52' 11.9309" S, 47° 41' 28.2768" W	32	130	30306	31	26
57	0° 52' 12.4626" S, 47° 41' 29.3406" W	25	100	16939	25	23
58	0° 52' 13.1912" S, 47° 41' 29.8982" W	32	100	16939	20	28
59	0° 52' 09.45" S / 47° 41' 25.96" W	32	130	30306	20	28
60	0° 51' 59.60" S / 47° 41' 23.67" W	25	120	25450	10	4
61	0° 51' 20.2196" S/ 47° 41' 40.5947" W	40	174	55968	17	0
62	0° 50' 40.3364" S/ 47° 41' 13.5287" W	26	120	25450	18	22
63	0° 51' 06.4462" S/ 47° 40' 47.6821" W	32	150	41143	25	26

Tabela 3.2- Geographic coordinates (latitude, longitude), tree height obtained by UAV (m), diameter at breast height (DBH, cm), above-ground biomass (AGB) and tree heights based on SRTM and TanDEM-X models for each sampled Rhizophora individual. AGB values were calculated using the allometric equations of Komiyama *et al.*(2008)

GCP	LAT/LONG	HEIGHT UAV (M)	DBH (CM)	BIOMASS(KG) (KOMIYAMA *ET AL.*, 2008)	HEIGHT (SRTM)	HEIGHT (TANDE)
1	0° 41' 17.6745" S, 47° 38' 28.7020" W	33	61	5569	20	30
2	0° 41' 20.6189" S, 47° 38' 28.1004" W	31	58	4919	23	30
3	0° 41' 18.6389" S, 47° 38' 29.4043" W	24	40	1972	18	25
4	0° 41' 17.0160" S, 47° 38' 25.5365" W	27	50	3414	20	22
5	0° 41' 18.5330" S, 47° 38' 27.3833" W	25	25	620	20	25
6	0° 41' 47.6942" S, 47° 38' 47.3996" W	32	60	5347	15	11
7	0° 41' 47.8890" S, 47° 38' 48.0784" W	20	30	971	17	16
8	0° 41' 47.8890" S, 47° 38' 48.0784" W	20	33	1228	16	11
9	0° 41' 47.9539" S, 47° 38' 48.2724" W	21	30	971	17	24
10	0° 41' 48.0514" S, 47° 38' 48.4664" W	23	41	2095	19	23
11	0° 41' 47.7586" S, 47° 38' 48.5308" W	27	48	3088	18	23
12	0° 41' 48.0512" S, 47° 38' 48.8219" W	26	50	3414	19	23
13	0° 41' 47.8886" S, 47° 38' 48.7895" W	21	36	1522	19	23
14	0° 41' 48.4743" S, 47° 38' 48.5636" W	24	29	894	19	25
15	0° 41' 48.6046" S, 47° 38' 48.4020" W	30	57	4713	20	25
16	0° 41' 48.2139" S, 47° 38' 48.8220" W	26	40	1972	20	25
17	0° 41' 48.4091" S, 47° 38' 48.9514" W	24	32	1139	20	25
20	0° 41' 51.9503" S, 47° 38' 58.0029" W	25	44	2493	11	25
21	0° 41' 51.6575" S, 47° 38' 57.9704" W	22	21	404	08	25
22	0° 41' 51.5926" S, 47° 38' 57.6795" W	10	9	50	09	25
23	0° 41' 51.6902" S, 47° 38' 57.7119" W	11	12	102	10	20
25	0° 41' 51.9179" S, 47° 38' 57.7120" W	18	23.6	538	12	25
26	0° 41' 51.6904" S, 47° 38' 57.2917" W	22	27	750	13	25
28	0° 41' 51.6254" S, 47° 38' 57.1301" W	26	43	2356	14	28
29	0° 41' 25.6028" S, 47° 38' 47.2257" W	33	54	4126	21	29
30	0° 41' 25.5701" S, 47° 38' 47.4843" W	30	48	3088	22	29
31	0° 41' 25.6026" S, 47° 38' 47.4843" W	31	48	3088	22	29
32	0° 41' 25.4723" S, 47° 38' 47.8397" W	28	36	1522	22	28
33	0° 41' 25.4399" S, 47° 38' 47.5165" W	29	37	1628	22	28
34	0° 41' 25.4725" S, 47° 38' 47.4196" W	30	46	2781	22	28

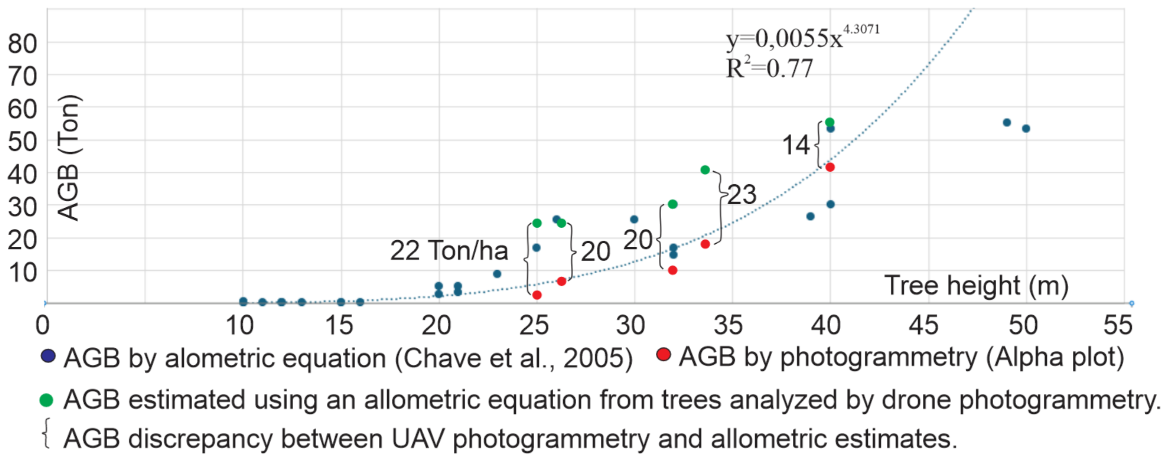

Figura 3.15- Exponential relationship between tree height (m) and above-ground biomass (AGB) for individual Avicennia trees. AGB was estimated from DBH using Chave *et al.* (2005, see Table 1). The fitted exponential equation and R^2 (obtained from the fit to the blue points) are shown on the plot. Blue points = data used to fit the model; red and green points = independent validation data.

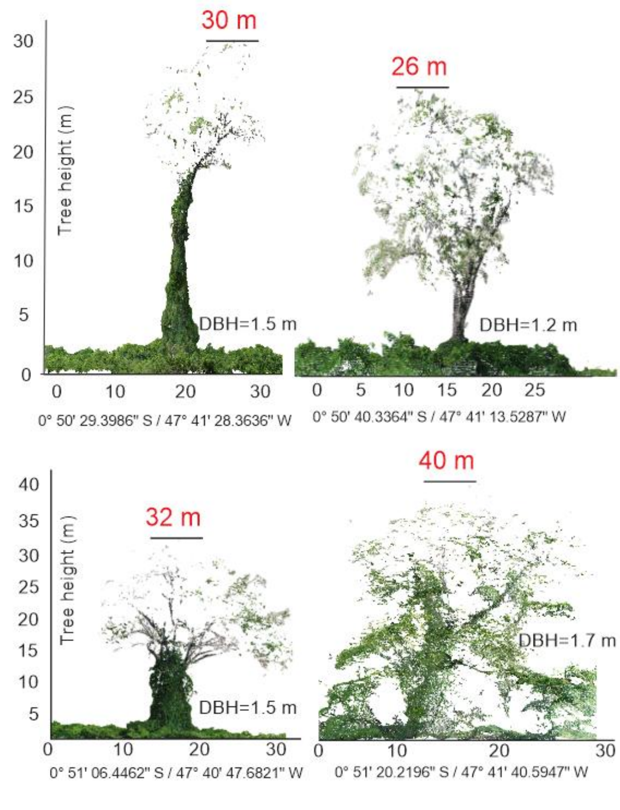

Figura 3.16- Detailed photogrammetric product derived from UAV imagery with individual tree height and diameter at breast height (DBH) measurements extracted from the 3D point cloud and in situ measures. The reconstructed 3D models were used to estimate woody volume

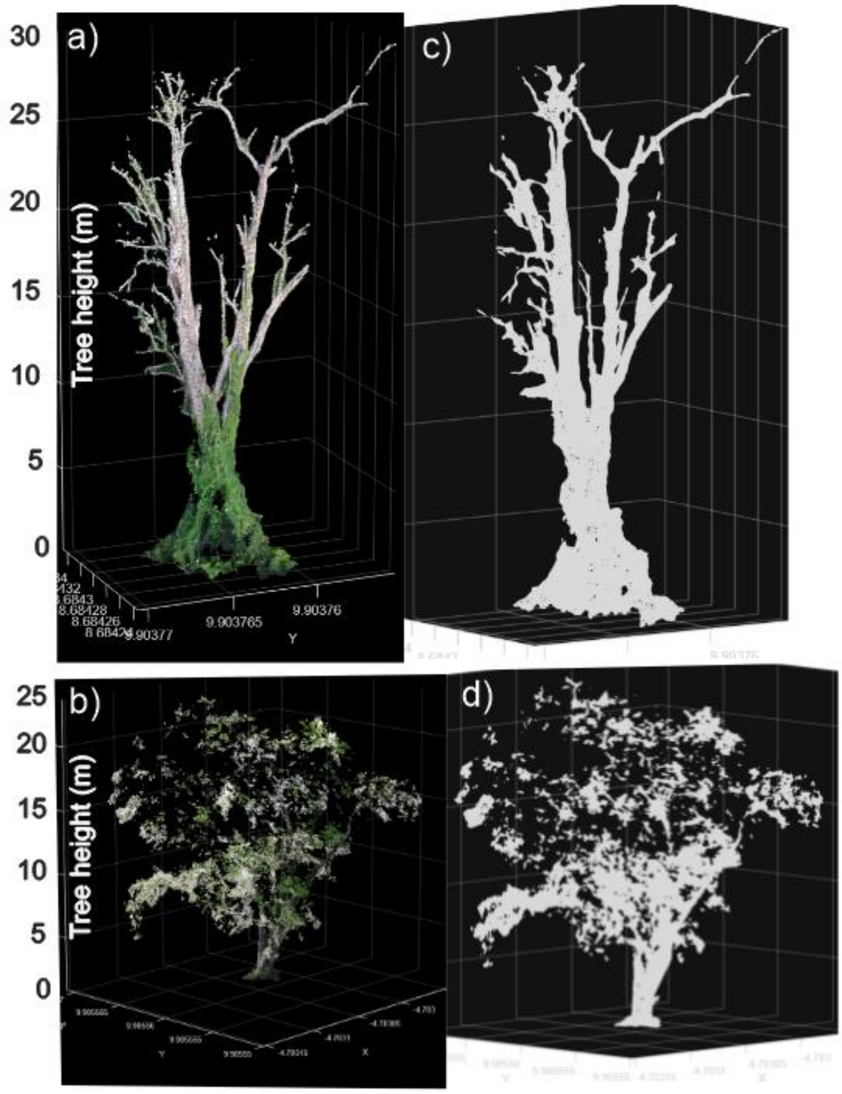

Figura 3.17- 3D models of two representative trees: (a) model without leaves, (b) model with leaves, and (c and d) alpha-shape envelopes (alpha-plot) showing the computed volume of each tree. Volumes were derived from alpha-shape hulls. See Methods for details.

3.6.1 Comparison of satellite and UAV-derived canopy height and biomass estimates

To evaluate accuracy and vertical discrepancies, digital elevation models obtained from SRTM and TanDEM-X were compared against high-resolution UAV-based elevation data (Tables 3.1 and 3.2). The studied mangrove forest typically occurs in a vertical range relative to mean sea level, generally between –2 and +3 m. Because SRTM-derived DEMs primarily capture the height of the mangrove canopy rather than the elevation of the underlying substrate, they do not provide true ground elevation within vegetated tidal flats. Consequently, local variations in the elevation of mangrove tidal plains—whether due to sediment deposition, erosion, or geomorphic gradients—can influence the apparent canopy height when estimated from SRTM data. In areas where the substrate is slightly elevated, SRTM may overestimate canopy height, whereas in subsided or lower-elevation zones, it may underestimate true canopy stature. This limitation highlights the importance of integrating UAV and local topographic surveys to accurately resolve mangrove height and structure. Considering this limitation, the SRTM model systematically underestimated *Rhizophora* canopy heights by an average of 7.4 m (Table 3.3) due to coarse resolution and deeper canopy penetration of the C-band signal. TanDEM-X (X-band), with finer spatial resolution and stronger interaction with upper foliage, showed much smaller bias (~0.6 m) and best captured heights in the dense northern sector. Consequently, TanDEM-X demonstrated much closer agreement with field-measured heights in the northern studied area. In the southern sector, however, structural heterogeneity reduced X-band coherence, shifting the phase center downward and resulting in underestimates for tall, sparsely spaced *Avicennia* (−5 to −6 m, Table 4). These outcomes reflect fundamental wavelength-dependent radar–vegetation interactions (Stovall *et al.*, 2021; Wessel *et al.*, 2018). AGB estimates mirrored these height patterns. TanDEM-X retrieved higher canopy heights than SRTM across most of the region, producing higher AGB (136 vs. 70 Mg ha^{-1}) using the same tree density derived from QuickBird imagery (Fig. 3.3).

Tabela 3.3- Error metrics (BIAS, MAE, and RMSE) comparing canopy height estimates derived from SRTM and TanDEM-X models against reference field measurements for *Rhizophora* stands. Negative BIAS values indicate a general underestimation of canopy height relative to the ground-truth data. The TanDEM-X model showed substantially lower error magnitudes and bias than SRTM, reflecting its higher spatial resolution and improved sensitivity to upper canopy surfaces.

Model	BIAS (m)	MAE (m)	RMSE (m)
SRTM	−7.37	7.37	8.35
TanDEM-X	−0.63	3.77	5.90

Tabela 3.4- Error metrics (BIAS, MAE, and RMSE) comparing canopy height estimates derived from SRTM and TanDEM-X models against reference field measurements for Avicennia stands. Negative BIAS values indicate a general underestimation of canopy height relative to the ground-truth data.

Model	BIAS (m)	MAE (m)	RMSE (m)
SRTM	−5.79	5.79	8.82
TanDEM-X	−5.64	5.82	10.50

3.6.2 Local-scale variability in mangrove structure and biomass

3.6.2.1 Structural patterns in the northern sector

UAV-based canopy height models revealed a broader and more realistic height distribution for both *Avicennia* and *Rhizophora* in the northern sector, reflecting the structural complexity of mature mangrove stands. The higher mean and maximum heights observed in UAV data (up to 34 m) contrast sharply with the smoother, lower distributions from SRTM and TanDEM-X, which underestimate canopy peaks due to their coarser spatial resolution and mixed ground–canopy returns (Simard *et al.*, 2019, 2025). The high spatial detail of UAV photogrammetry (~3 cm GSD) enables precise delineation of individual crowns and canopy gaps, resulting in more accurate estimates of height and above-ground biomass (AGB). UAV-derived AGB (430 Mg ha^{-1}) was more than double that derived from SRTM (201 Mg ha^{-1}) and significantly higher than TanDEM-X (220 Mg ha^{-1}), confirming that radar-based DEMs smooth canopy structure and underestimate total carbon stocks (Fatoyinbo *et al.*, 2018; Lucas *et al.*, 2020). Nonetheless, TanDEM-X provided a more accurate vertical representation than SRTM, capturing a greater proportion of mid- to upper-canopy classes, consistent with its finer spatial resolution (12 m) and enhanced interferometric sensitivity (Rizzoli *et al.*, 2017). These results emphasize the critical role of UAV-based observations in quantifying canopy variability and biomass in structurally complex mangrove forests.

3.6.2.2 Structural patterns in the southern sector

The southern sector contained the tallest mangroves (49–53 m) and the highest AGB (~648 Mg ha^{-1}) according to UAV photogrammetry. The UAV-based histogram showed a flattened rather than a classic stepped pattern between the classes 16 and 30 m (Fig. 3.9), likely due to mechanical stress and crown breakage caused by strong coastal winds, as observed in defoliated or damaged trees near exposed margins. Some *Avicennia* trees with DBH ≥ 1 m were observed despite being only ~25 m tall (Table 3.1). This pattern suggests the presence of old individuals that may have lost their upper crowns due to strong wind events, resulting in reduced overall height despite large trunk diameters. SRTM and GLO-30 DEM/TanDEM-X underestimated height and AGB estimates (207 and 30 Mg ha^{-1}, respectively), severely in this sector due to sparse spacing and heterogeneous vegetation.

3.6.3 AGB discrepancies among UAV, SRTM, and TanDEM-X datasets

The differences among UAV-, SRTM-, and TanDEM-X-derived AGB arise from both temporal and methodological factors.

1. Acquisition date: SRTM (2000) and TanDEM-X (2011–2013) predate the UAV surveys (2024–2025), and thus do not reflect forest growth, regeneration, or disturbance recovery over the past two decades.

2. Spatial resolution: The coarser pixel sizes of SRTM (30 m) and TanDEM-X (12 m) average canopy and ground signals, especially along creeks, gaps, and water edges, which depress effective heights.

3. Radar signal penetration and coherence: SRTM's C-band (λ ≈ 5.6 cm) penetrates deeper into vegetation, placing its interferometric phase center typically 5–10 m below the canopy top, depending on forest density and moisture (Simard *et al.*, 2025). TanDEM-X's X-band (λ ≈ 3 cm) is more sensitive to fine canopy surfaces but highly dependent on local backscatter coherence. Dense, homogeneous canopies, such as those in the northern sector, produce coherent returns closer to the canopy top, yielding higher height estimates than those from SRTM. In contrast, structurally irregular stands with large gaps and mixed vegetation—typical of the southern sector—induce signal decorrelation and shadowing, causing the radar phase center to shift downward within the canopy

   (Huber *et al.*, 2012; Stovall *et al.*, 2021).

4. Sensor geometry: The near-horizontal bistatic baseline of TanDEM-X amplifies the effect of layover and shadowing on steep or irregular surfaces, enhancing underestimation in open or wind-exposed mangrove zones (Lee *et al.*, 2018; Lucas *et al.*, 2020; Wessel *et al.*, 2018). Then, in the southern study area, TanDEM-X significantly underestimates *Avicennia* canopy heights (−10 m, Table 4), likely due to the more open canopy architecture in the southern study area. Together, these findings highlight the extent to which species-specific canopy structure shapes radar–vegetation interactions, ultimately influencing DEM performance in mangrove ecosystems.

By contrast, UAV photogrammetry reconstructs the true top-of-canopy envelope from overlapping nadir and oblique imagery with centimeter-level precision (Wang *et al.*, 2019), resolving emergent crowns and dominant individuals that disproportionately contribute to AGB (Fatoyinbo *et al.*, 2018; Simard *et al.*, 2019a). In addition, UAV-based orthomosaics with a ground resolution of approximately 3 cm substantially improve the delineation of mangrove areas and the estimation of tree density. These high-resolution products allow the identification of individual crowns, canopy gaps, and fine-scale stand boundaries that are not detectable in satellite imagery. Because tree density, mangrove area, and canopy height are as critical to biomass estimation as the choice of allometric equations, the enhanced spatial detail provided by UAV orthomosaics and DEMs is key to producing more accurate, spatially explicit AGB assessments. Therefore, integrating SRTM, TanDEM-X, and UAV data provides complementary insights: regional mapping from radar DEMs and fine-scale calibration from UAV surveys together enable accurate characterization of mangrove height dynamics and carbon stocks across heterogeneous landscapes.

3.6.4 Global context of mangrove canopy height and biomass

To our knowledge, no previous study has documented mangrove canopies exceeding 30 m in Brazil; therefore, the 49–53 m heights reported here constitute the first evidence of truly tall mangrove systems in the Amazonian coastal domain, placing this site among the tallest mangrove forests documented globally. These values align with global assessments using SRTM, GEDI, and TanDEM-X, which identify the highest canopies in the Americas (e.g., Colombia ~54 m; Venezuela ~52.6 m; Panama ~50.9 m) and in West-Central Africa (Gabon ~62.8 m) (Simard *et al.*, 2019). A new global 12-m mangrove height product derived from TanDEM-X and calibrated with GEDI further confirms near-60-m stands in Gabon and Colombia, with detailed mapping of tall patches (Simard *et al.*, 2025). Our canopy height maximum (53 m), therefore, falls within the upper envelope of mangrove heights observed across the tropics.

Regionally, mangrove stature varies considerably. The tallest Neotropical canopies (>50 m) occur along the Colombian Pacific coast, where field and UAV surveys report maxima of 54–58 m, while stands in Pongara National Park (Gabon) regularly exceed 60 m (Castellanos-Galindo *et al.*, 2021). In contrast, Asian mangroves generally show lower stature (e.g., China: mean 6–10 m; maxima <10 m in species-level maps), reflecting differences in biogeography, climate, and disturbance regimes (R. Chen *et al.*, 2023; Simard *et al.*, 2025). In Brazil, earlier studies report localized patches reaching 20–30 m tall in Amazonian estuaries (Cohen *et al.*, 2018; Cohen & Lara, 2003; Menezes *et al.*, 2008)—highlighting the exceptional nature of our 49–53 m canopy heights.

Regarding biomass, global compilations show that low (5 – 10 m) and mean (10 – 20 m) mangroves present AGB of 20-80 Mg ha^{-1} and 100-200 Mg ha^{-1}, respectively, and very tall mangrove stands (20 – 40 m) often support extremely high AGB (>300–500 Mg ha^{-1}), with hotspots approaching ~800 Mg ha^{-1} in the tallest forests, while global means remain lower (100 – 300 Mg ha^{-1}) (Hu *et al.*, 2020; Komiyama *et al.*, 2008). According to the global mangrove AGB assessment by Hu *et al.* (2020), Brazilian mangrove forests exhibit moderate to high biomass values relative to global patterns. Their 30-m AGB map shows that most stands along the northern Pará–Amapá coast fall within the ~150–300 Mg ha^{-1} range. Our UAV-based measurements indicated AGB ranging from ~450 to ~650 Mg ha^{-1} and localized sectors reaching up to 800 Mg ha^{-1}. Given that the global mean mangrove AGB is approximately 115 Mg ha^{-1}, these values place much of the Brazilian northern macrotidal mangrove belt well above the global average.

Therefore, Brazil is recognized as a blue-carbon hotspot due to its extensive mangrove area and pronounced spatial heterogeneity (Rovai *et al.*, 2022). Within this global framework, the combination of very tall canopy percentiles and our plot-to-height scaling indicates that the study area occupies the upper tail of AGB distributions, consistent with the most carbon-dense tall-mangrove systems (Komiyama *et al.*, 2008). The agreement between our UAV-derived canopy maximum (53 m) and global mangrove height limits supports the interpretation that this site hosts exceptionally tall mangroves and functions as a blue-carbon hotspot by both Brazilian and international standards.

3.7 CONCLUSIONS

This study demonstrates that radar-derived digital elevation models (DEMs), commonly used in Earth observation–based vegetation analyses, systematically underestimate canopy height and AGB in tall, structurally heterogeneous mangrove forests. Sensor-dependent biases are strongly controlled by canopy architecture, spatial heterogeneity, and radar–vegetation interactions. While TanDEM-X generally outperforms SRTM in dense, vertically homogeneous stands, both products fail to capture canopy peaks and emergent trees, which disproportionately contribute to biomass and carbon stocks in open, irregular, or wind-disturbed mangrove systems.

By integrating wall-to-wall satellite DEMs with ultra–high-resolution UAV-based photogrammetry, we introduce a robust calibration and validation framework that improves canopy height retrieval and biomass estimation across complex coastal landscapes. UAV-derived structural metrics effectively constrain sensor biases, resolve fine-scale canopy variability, and enable more accurate upscaling of field-based allometric relationships to landscape scales. This multi-sensor approach highlights the limitations of relying solely on satellite-derived elevation products for biomass estimation in heterogeneous forests and underscores the importance of UAV-assisted calibration in Earth observation workflows.

Beyond revealing that Amazonian mangroves rank among the tallest and most carbon-dense mangrove systems globally, our results demonstrate that current global and regional EO products likely underestimate both canopy height and carbon stocks in similar tall, heterogeneous coastal forests. The canopy heights reported here (up to 53 m) and associated biomass values (locally approaching ~800 Mg ha^{-1}) place the study area within the upper envelope of global mangrove structure and carbon density, emphasizing its role as a blue-carbon hotspot.

More broadly, this work advances applied Earth observation by providing a transferable multi-sensor data fusion framework that can be applied to other forested and coastal environments where satellite-based products alone remain insufficient. Integrating UAV photogrammetry with spaceborne radar and elevation datasets offers a practical pathway to improve vegetation structure retrieval, reduce uncertainty in biomass mapping, and enhance the reliability of EO-based environmental modelling and carbon assessments at regional to global scales.

4. CONSIDERAÇÕES FINAIS

Foi estimada a altura do dossel e a biomassa aérea (AGB) dos manguezais do Estuário do Rio Marapanim, no nordeste do estado do Pará, Brasil, a fim de avaliar o papel desses ecossistemas como áreas de elevado acúmulo de carbono. Os resultados mostraram que as formações arbóreas presentes nos setores norte e sul atingem alturas excepcionais, chegando a 53 m, valores que figuram entre os mais elevados já registrados no Brasil e se aproximam daqueles observados em alguns dos manguezais mais altos do mundo. Da mesma forma, a biomassa aérea estimada ultrapassou 600 Mg/ha, situando-se acima das médias globais de florestas de mangue.

As estimativas obtidas a partir dos dados TanDEM-X, SRTM/GLO-30 e dos produtos fotogramétricos de VANT mostraram-se complementares para caracterizar a estrutura do dossel e a distribuição espacial da biomassa. Contudo, as diferenças de resolução entre os sensores geraram contrastes expressivos nas alturas e nos valores de AGB, sendo os dados provenientes de VANT os que apresentaram maior precisão e capacidade de representar a variabilidade estrutural da floresta. Em áreas de difícil acesso, onde a mensuração direta do DAP não é viável, os sobrevoos com VANT demonstraram-se a ferramenta mais adequada para a aquisição de informações estruturais detalhadas. Embora os resultados sejam robustos, ressalta-se que as estimativas ainda estão condicionadas à disponibilidade de dados de campo e à resolução espacial dos sensores utilizados

A formulação de equações empíricas ajustadas com dados locais, baseadas em modelos alométricos consolidados, permitiu estimar a biomassa aérea com maior detalhamento e coerência com as características específicas do ERM. Essas equações, aliadas aos modelos digitais gerados pelos VANTs, também permitiram delimitar com maior precisão a extensão real das áreas de mangue, além de identificar feições geomorfológicas relevantes, como canais de maré e zonas de transição na planície intermaré.

Uma delimitação mais precisa dos manguezais não apenas atualiza o inventário do estuário do Rio Marapanim, como também contribui para o conhecimento sobre o maior cinturão contínuo de manguezais do mundo. Além disso, destaca setores com árvores de grande porte e elevado DAP, identificando áreas com potencial significativo de armazenamento de carbono que merecem ser analisadas sob a ótica de sua dinâmica ambiental e biogeoquímica.

Os resultados apresentados reforçam a necessidade de integrar tecnologias de alta resolução, como os VANTs, no monitoramento dos manguezais amazônicos. Esses dados são essenciais para a calibração de novos produtos orbitais voltados à estimativa global de biomassa florestal, como a missão BIOMASS da Agência Espacial Europeia, e para aprimorar os mapas de carbono em regiões onde a complexidade estrutural do dossel impõe desafios aos sensores satelitais. Em conjunto, os achados confirmam a importância do ERM como área estratégica para compreender a dinâmica do carbono azul e subsidiar ações de conservação e mitigação diante das mudanças climáticas. Assim, o ERM se consolida como uma área-chave para estudos integrados sobre carbono azul, fornecendo subsídios científicos para estratégias de conservação, manejo e mitigação das mudanças climáticas em ambientes costeiros tropicais.

REFERÊNCIAS

Alongi D. M. 2002. Present state and future of the world's mangrove forests. *Environmental Conservation,* **29** (3): 331–349). https://doi.org/10.1017/S0376892902000231

Alongi D. M. 2008. Mangrove forests: resilience, protection from tsunamis, and responses to global climate change. *Estuarine, Coastal and Shelf Science,* **76** (1):1–13. https://doi.org/10.1016/j.ecss.2007.08.024

Alongi D. M. 2015. The impact of climate change on mangrove forests. *Current Climate Change Reports,* **1** (1): 30–39. Springer. https://doi.org/10.1007/s40641-015-0002-x

Alongi D. M. 2020. Global significance of mangrove blue carbon in climate change mitigation. *Sci*, **2**(3): 67–60. https://doi.org/10.3390/SCI2030067

Alongi D. M. 2022. Climate change and mangroves. *In*: Das S. C., Pullaiah T., Ashton E. C. (eds.). *Mangroves:* biodiversity, livelihoods and conservation. Singapore, Springer. p. 175–198. https://doi.org/10.1007/978-981-19-0519-3_8/COVER

Atwood T. B., Connolly R. M., Almahasheer H., Carnell P. E., Duarte C. M., Lewis C. J. E., Irigoien X., Kelleway J. J., Lavery P. S., Macreadie P. I., Serrano O., Sanders C. J., Santos I., Steven A. D. L., Lovelock C. E. 2017. Global patterns in mangrove soil carbon stocks and losses. *Nature Climate Change*, **7**(7): 523–528. https://doi.org/10.1038/nclimate3326

Baccini A., Goetz S. J., Walker W. S., Laporte N. T., Sun M., Sulla-Menashe D., Hackler J., Beck P. S. A., Dubayah R., Friedl M. A., Samanta S., Houghton R. A. 2012. Estimated carbon dioxide emissions from tropical deforestation improved by carbon-density maps. *Nature Climate Change*, **2**(3): 182–185. https://doi.org/10.1038/nclimate1354

Ball M.C. 1988. Ecophysiology of mangroves. *Trees* **2**: 129–142. https://doi.org/10.1007/BF00196018

Bernardino A. F., Mazzuco A. C. A., Costa R. F., Souza F., Owuor M. A., Nobrega G. N., Sanders C. J., Ferreira T. O., Kauffman J. B. 2024. The inclusion of Amazon mangroves in Brazil's REDD+ program. *Nature Communications*, **15**(1): 1549. https://doi.org/10.1038/s41467-024-45459-w

Berrêdo J. F., Costa M. L., Progene M. D. P. S. 2008. Efeitos das variações sazonais do clima tropical úmido sobre as águas e sedimentos de manguezais do estuário do rio Marapanim, costa nordeste do Estado do Pará. *Acta Amazonica*, **38**(3): 473–482. https://doi.org/10.1590/S0044-59672008000300012

Bhatia K. T., Vecchi G. A., Knutson T. R., Murakami H., Kossin J., Dixon K. W., Whitlock C. E. 2019. Recent increases in tropical cyclone intensification rates. *Nature Communications*, **10**(1): 635. https://doi.org/10.1038/s41467-019-08471-z

Bird E. 2008. *Coastal geomorphology :* an introduction. [*S.l.*], Wiley.

Blasco F., Saenger P., Janodet E.. 1996. Mangroves as indicators of coastal change, *Catena*, **27**(3–4):167-178,ISSN 0341-8162, https://doi.org/10.1016/0341-8162(96)00013-6.

Cardenas, S. M. M., Cohen, M. C. L., Ruiz, D. P. C., Souza, A. V., Gomez-Neita, J. S., Pessenda, L. C. R., & Culligan, N. (2022). Death and regeneration of an Amazonian mangrove forest by anthropic and natural forces. *Remote Sensing*, *14*(24). https://doi.org/10.3390/rs14246197

Castellanos-Galindo, G. A., Casella, E., Tavera, H., Zapata Padilla, L. A., & Simard, M. (2021). Structural characteristics of the tallest mangrove forests of the american continent: a comparison of ground-based, drone and radar measurements. *Frontiers in Forests and Global Change*, *4*. https://doi.org/10.3389/ffgc.2021.732468

Chave, J., Andalo, A. C., Brown, A. S., Cairns, A. M. A., Chambers, J. Q., Eamus, A. D., Foïster, A. H., Fromard, A. F., Higuchi, N., Kira, A. T., Lescure, J.-P., Nelson, A. B. W., Ogawa, H., Puig, A. H., Rie´ra, A. B., Ae, R., Yamakura, T., Brown, S., Cairns, M. A., … Rie´ra, B. R. (2005). *Tree allometry and improved estimation of carbon stocks and balance in tropical forests*. https://doi.org/10.1007/s00442-005

Chen, R., Zhang, R., Zhao, C., Wang, Z., & Jia, M. (2023). High-resolution mapping of mangrove species height in Fujian Zhangjiangkou national mangrove nature reserve combined GF-2, GF-3, and UAV-LiDAR. *Remote Sensing*, *15*(24). https://doi.org/10.3390/rs15245645

Chen, Y.-J., Liao, B.-W., Li, M., Chen, B.-F., Chen, Y.-H., Zhong, C.-R., Li, H.-L., & Lin, W.-H. (2012). Wind-attenuation effect of *Sonneratia apetala* and *Kandelia obovata* plantations. *Ying Yong Sheng Tai Xue Bao = The Journal of Applied Ecology*, *23*(4), 959–964.

Cohen, M. C. L., Behling, H., & Lara, R. J. (2005). Amazonian mangrove dynamics during the last millennium: The relative sea-level and the Little Ice Age. *Review of Palaeobotany and Palynology*, *136*(1–2), 93–108. https://doi.org/10.1016/j.revpalbo.2005.05.002

Cohen, M. C. L., de Souza, A. V., Rossetti, D. F., Pessenda, L. C. R., & França, M. C. (2018). Decadal-scale dynamics of an Amazonian mangrove caused by climate and sea level changes: inferences from spatial–temporal analysis and digital elevation models. *Earth Surface Processes and Landforms*, *43*(14), 2876–2888. https://doi.org/10.1002/ESP.4440

Cohen, M. C. L., Fontes, N. A., Rodrigues, E., Pessenda, L. C. R., França, M. C., Garrett, E., & Ryu, J. (2025). Squeeze of Brazilian subtropical mangroves from a Holocene and Anthropocene perspective. *CATENA*, *260*, 109450. https://doi.org/10.1016/j.catena.2025.109450

Cohen, M. C. L., Pessenda, L. C. R., Behling, H., de Fátima Rossetti, D., França, M. C., Guimarães, J. T. F., Friaes, Y., & Smith, C. B. (2012). Holocene palaeoenvironmental history of the Amazonian mangrove belt. *Quaternary Science Reviews*, *55*, 50–58. https://doi.org/10.1016/j.quascirev.2012.08.019

Cohen, M. C. L., Ruiz, D. P. C., Rodrigues, E., Yao, Q., de Souza, A. V., Liu, K., Pessenda, L. C. R., Aragón-Moreno, A. A., Ryu, J., & Nunes, S. (2024). Florida mangrove dieback on a decadal and centennial timescales. *Science of The Total Environment*, *956*, 177345. https://doi.org/10.1016/j.scitotenv.2024.177345

Cohen, M. C. L., Souza Filho, P. W. M., Lara, R. J., Behling, H., & Angulo, R. J. (2005). A model of Holocene mangrove development and relative sea-level changes on the Bragança Peninsula (northern Brazil). *Wetlands Ecology and Management*, *13*(4), 433–443. https://doi.org/10.1007/s11273-004-0413-2

Cohen, M. C. L., Yao, Q., de Souza, A. V., Liu, K. biu, & Pessenda, L. C. R. (2024). Hurricanes are limiting the mangrove canopy heights in the Gulf of Mexico. *Science of the Total Environment*, *927*. https://doi.org/10.1016/j.scitotenv.2024.172284

Cohen, M., & Lara, R. (2003). Temporal changes of mangrove vegetation boundaries in Amazônia: Application of GIS and remote sensing techniques. *Wetlands Ecology and Management*, *11*(4), 223–231. https://doi.org/10.1023/A:1025007331075

Das, S., & Crépin, A. S. (2013). Mangroves can provide protection against wind damage during storms. *Estuarine, Coastal and Shelf Science*, *134*, 98–107. https://doi.org/10.1016/j.ecss.2013.09.021

David, H. C., Vibrans, A. C., Martins-Neto, R. P., Dalla Corte, A. P., & Péllico Netto, S. (2024). Incorporating forest mapping-related uncertainty into the error propagation of wall-to-wall biomass maps: a general approach for large and small areas. *Remote Sensing*, *16*(22), 4295. https://doi.org/10.3390/rs16224295

Donato, D. C., Kauffman, J. B., Murdiyarso, D., Kurnianto, S., Stidham, M., & Kanninen, M. (2011). Mangroves among the most carbon-rich forests in the tropics. *Nature Geoscience*, *4*(5), 293–297. https://doi.org/10.1038/ngeo1123

Fatoyinbo, T., Feliciano, E. A., Lagomasino, D., Lee, S. K., & Trettin, C. (2018). Estimating mangrove aboveground biomass from airborne LiDAR data: a case study from the Zambezi River delta. *Environmental Research Letters*, *13*(2), 025012. https://doi.org/10.1088/1748-9326/aa9f03

Fernandes M. E. B. 2016. Os manguezais da costa Norte brasileira. [*S.l.*], *Laboratório de Ecologia de Manguezal*. v.3. Disponível em: http://www.ufpa.br/lama. Acesso em 12 de dezembro de 2025.

Fernandes M. E. B., Proisy C., Oyedotun T. D., Djosetro M., Ximenes A. C., Souza-Filho P. W. M.e, Gomes C. P., Virgulino-Júnior P. C.C., Gomes V. J.C., Suárez E. L., Gregor S. G. 2025. *Mangroves of the North Brazil shelf*. Disponível em: www.iucnrle.org. Acesso em 12 de dezembro de 2025.

Fitzjarrald, D. R., Sakai, R. K., Moraes, O. L. L., Cosme de Oliveira, R., Acevedo, O. C., Czikowsky, M. J., & Beldini, T. (2008). Spatial and temporal rainfall variability near the Amazon-Tapajós confluence. *Journal of Geophysical Research: Biogeosciences*, *113*(G1). https://doi.org/10.1029/2007JG000596

França, M. C., Pessenda, L. C. R., Cohen, M. C. L., de Azevedo, A. Q., Fontes, N. A., Silva, F. B., de Melo, J. C. F., Piccolo, M. de C., Bendassolli, J. A., & Macario, K. (2019). Late-Holocene subtropical mangrove dynamics in response to climate change during the last millennium. *Holocene*, *29*(3), 445–456. https://doi.org/10.1177/0959683618816438

Friedlingstein, P., O'Sullivan, M., Jones, M. W., Andrew, R. M., Bakker, D. C. E., Hauck, J., Landschützer, P., Le Quéré, C., Luijkx, I. T., Peters, G. P., Peters, W., Pongratz, J., Schwingshackl, C., Sitch, S., Canadell, J. G., Ciais, P., Jackson, R. B., Alin, S. R., Anthoni, P., … Zheng, B. (2023). Global carbon budget 2023. *Earth System Science Data*, *15*(12), 5301–5369. https://doi.org/10.5194/essd-15-5301-2023

Fromard, F., Puig, H., Mougin, E., Marty, G., Betoulle, J. L., & Cadamuro, L. (1998). Structure, above-ground biomass and dynamics of mangrove ecosystems: New data from French Guiana. *Oecologia, 115*(1–2), 39–53. https://doi.org/10.1007/s004420050489

Gatti, L. V., Basso, L. S., Miller, J. B., Gloor, M., Gatti Domingues, L., Cassol, H. L. G., Tejada, G., Aragão, L. E. O. C., Nobre, C., Peters, W., Marani, L., Arai, E., Sanches, A. H., Corrêa, S. M., Anderson, L., Von Randow, C., Correia, C. S. C., Crispim, S. P., & Neves, R. A. L. (2021). Amazonia as a carbon source linked to deforestation and climate change. *Nature*, *595*(7867), 388–393. https://doi.org/10.1038/s41586-021-03629-6

Ghosh, S. M., Behera, M. D., & Paramanik, S. (2020). Canopy height estimation using sentinel series images through machine learning models in a Mangrove Forest. *Remote Sensing*, *12*(9). https://doi.org/10.3390/RS12091519

Gilman, E. L., Ellison, J., Duke, N. C., & Field, C. (2008). Threats to mangroves from climate change and adaptation options: A review. In *Aquatic Botany* (Vol. 89, Issue 2, pp. 237–250). https://doi.org/10.1016/j.aquabot.2007.12.009

Hermann Behling, P.-D. (2002). Impact of the Holocene sea-level changes in coastal, eastern and Central Amazonia (Issue 112). Kiel.

Hirata, Y., Tabuchi, R., Patanaponpaiboon, P., Poungparn, S., Yoneda, R., & Fujioka, Y. (2014). Estimation of aboveground biomass in mangrove forests using high-resolution satellite data. *Journal of Forest Research*, *19*(1), 34–41. https://doi.org/10.1007/s10310-013-0402-5

Hsu, A. J., Kumagai, J., Favoretto, F., Dorian, J., Guerrero Martinez, B., & Aburto-Oropeza, O. (2020). Driven by Drones: Improving mangrove extent maps using high-resolution remote sensing. *Remote Sensing*, *12*(23), 3986. https://doi.org/10.3390/rs12233986

Hu, T., Zhang, Y., Su, Y., Zheng, Y., Lin, G., & Guo, Q. (2020). Mapping the global mangrove forest aboveground biomass using multisource remote sensing data. *Remote Sensing*, *12*(10), 1690. https://doi.org/10.3390/rs12101690

Hubau, W., Lewis, S. L., Phillips, O. L., Affum-Baffoe, K., Beeckman, H., Cuní-Sanchez, A., Daniels, A. K., Ewango, C. E. N., Fauset, S., Mukinzi, J. M., Sheil, D., Sonké, B., Sullivan, M. J. P., Sunderland, T. C. H., Taedoumg, H., Thomas, S. C., White, L. J. T., Abernethy, K. A., Adu-Bredu, S., … Zemagho, L. (2020). Asynchronous carbon sink saturation in African and Amazonian tropical forests. *Nature*, *579*(7797), 80–87. https://doi.org/10.1038/s41586-020-2035-0

Huber, M., Gruber, A., Wendleder, A., Wessel, B., Roth, A., & Schmitt, A. (2012). The global TanDEM-X DEM: production status and first validation results. *The International Archives of the Photogrammetry, Remote Sensing and Spatial Information Sciences*, *XXXIX-B7*, 45–50. https://doi.org/10.5194/isprsarchives-XXXIX-B7-45-2012

Hutchison, J., Manica, A., Swetnam, R., Balmford, A., & Spalding, M. (2014). Predicting global patterns in mangrove forest biomass. *Conservation Letters*, *7*(3), 233–240. https://doi.org/10.1111/conl.12060

Intergovernmental Panel on Climate Change IPCC. 2023. *Climate change 2021* – the physical science basis. Cambridge University Press. https://doi.org/10.1017/9781009157896

Jardine, S. L., & Siikamäki, J. V. (2014). A global predictive model of carbon in mangrove soils. *Environmental Research Letters*, *9*(10). https://doi.org/10.1088/1748-9326/9/10/104013

Kauffman, J. B., Bernardino, A. F., Ferreira, T. O., Giovannoni, L. R., De Gomes, L. E. O., Romero, D. J., Jimenez, L. C. Z., & Ruiz, F. (2018). Carbon stocks of mangroves and salt marshes of the Amazon region, Brazil. *Biology Letters*, *14*(9). https://doi.org/10.1098/rsbl.2018.0208

Kauffman, J. B., Fernanda Adame, M., Budi Arifanti, V., Schile-beers, L. M., Bernardino, A. F., Bhomia, R. K., Donato, D. C., Feller, I. C., Ferreira, T. O., Del Carmen Jesus Garcia, M., Mackenzie, R. A., Patrick Megonigal, J., Murdiyarso, D., Simpson, L., Hern Andez Trejo, H., Adame, M. F., Arifanti, V. B., Schile-Beers, L. M., Bernardino, A. F., … Simpson, L. (2020). Total ecosystem carbon stocks of mangroves across broad global environmental and physical gradients. 2020, 1405. https://doi.org/10.1002/ecm.1405

Knutson, T., Camargo, S. J., Chan, J. C. L., Emanuel, K., Ho, C. H., Kossin, J., Mohapatra, M., Satoh, M., Sugi, M., Walsh, K., & Wu, L. (2020). Tropical cyclones and climate change assessment part II: Projected response to anthropogenic warming. *Bulletin of the American Meteorological Society*, *101*(3), E303–E322. https://doi.org/10.1175/BAMS-D-18-0194.1

Komiyama, A., Ong, J. E., & Poungparn, S. (2008). Allometry, biomass, and productivity of mangrove forests: A review. In *Aquatic Botany* (Vol. 89, Issue 2, pp. 128–137). https://doi.org/10.1016/j.aquabot.2007.12.006

Komiyama, A., Poungparn, S., & Kato, S. (2005). Common allometric equations for estimating the tree weight of mangroves. *J Trop Ecol*, *21*(4), 471–477. https://doi.org/10.1017/s0266467405002476

Lacerda, L., Conde, J., Kjerfve, B., Alvarez-León, R., Alarcón, C., & Polanía, J. (2002). *American mangroves*. https://www.researchgate.net/publication/239557247

Lagomasino, D., Fatoyinbo, T., Castañeda-Moya, E., Cook, B. D., Montesano, P. M., Neigh, C. S. R., Corp, L. A., Ott, L. E., Chavez, S., & Morton, D. C. (2021). Storm surge and ponding explain mangrove dieback in Southwest Florida following hurricane Irma. *Nature Communications*, *12*(1). https://doi.org/10.1038/s41467-021-24253-y

Lagomasino, D., Fatoyinbo, T., Lee, S. K., Feliciano, E., Trettin, C., & Simard, M. (2016). A comparison of mangrove canopy height using multiple independent measurements from land, air, and space. *Remote Sensing 2016, Vol. 8, Page 327*, *8*(4), 327. https://doi.org/10.3390/RS8040327

Lähteenoja, O., Reátegui, Y. R., Räsänen, M., Torres, D. D. C., Oinonen, M., & Page, S. (2012). The large Amazonian peatland carbon sink in the subsiding Pastaza- Marañón foreland basin, Peru. *Global Change Biology*, *18*(1), 164–178. https://doi.org/10.1111/j.1365-2486.2011.02504.x

Lara, R. J., & Cohen, M. C. L. (2006). Sediment porewater salinity, inundation frequency and mangrove vegetation height in Bragança, North Brazil: An ecohydrology-based empirical model. *Wetlands Ecology and Management*, *14*(4), 349–358. https://doi.org/10.1007/s11273-005-4991-4

Lee, S.-K., Fatoyinbo, T. E., Lagomasino, D., Feliciano, E., & Trettin, C. (2018). Multibaseline TanDEM-X mangrove height estimation: the selection of the vertical wavenumber. *IEEE Journal of Selected Topics in Applied Earth Observations and Remote Sensing*, *11*(10), 3434–3442. https://doi.org/10.1109/JSTARS.2018.2835647

Lovelock, C. E., Feller, I. C., Reef, R., Hickey, S., & Ball, M. C. (2017). Mangrove dieback during fluctuating sea levels. *Scientific Reports*, *7*(1), 1680. https://doi.org/10.1038/s41598-017-01927-6

Lu, W., Chen, L., Wang, W., Fung-Yee Tam, N., & Lin, G. (2013). Effects of sea level rise on mangrove Avicennia population growth, colonization and establishment: Evidence from a field survey and greenhouse manipulation experiment. *Acta Oecologica*, *49*, 83–91. https://doi.org/10.1016/j.actao.2013.03.009

Lucas, R., Van De Kerchove, R., Otero, V., Lagomasino, D., Fatoyinbo, L., Omar, H., Satyanarayana, B., & Dahdouh-Guebas, F. (2020). Structural characterisation of mangrove forests achieved through combining multiple sources of remote sensing data. *Remote Sensing of Environment*, *237*, 111543. https://doi.org/10.1016/j.rse.2019.111543

Malhi, Y., Aragão, L. E. O. C., Galbraith, D., Huntingford, C., Fisher, R., Zelazowski, P., Sitch, S., McSweeney, C., & Meir, P. (2009). Exploring the likelihood and mechanism of a climate-change-induced dieback of the Amazon rainforest. *Proceedings of the National Academy of Sciences*, *106*(49), 20610–20615. https://doi.org/10.1073/pnas.0804619106

Matos, C. R. L., Berrêdo, J. F., Machado, W., Sanders, C. J., Metzger, E., & Cohen, M. C. L. (2020). Carbon and nutrient accumulation in tropical mangrove creeks, Amazon region. https://doi.org/10.1016/j.margeo.2020.106317

McLachlan, R. L., Ogston, A. S., Asp, N. E., Fricke, A. T., Nittrouer, C. A., & Gomes, V. J. C. (2020). Impacts of tidal-channel connectivity on transport asymmetry and sediment exchange with mangrove forests. *Estuarine, Coastal and Shelf Science*, 233, 106524. https://doi.org/10.1016/j.ecss.2019.106524

Menéndez, P., Losada, I. J., Torres-Ortega, S., Narayan, S., & Beck, M. W. (2020). The global flood protection benefits of mangroves. *Scientific Reports*, *10*(1). https://doi.org/10.1038/S41598-020-61136-6.

Menezes, P. M., Berger, U., & Mehlig, U. (2008). Mangrove vegetation in Amazonia: a review of studies from the coast of Pará and Maranhão States, north Brazil. *38*(3), 403–420.

Meng, Y., Bai, J., Gou, R., Cui, X., Feng, J., Dai, Z., Diao, X., Zhu, X., & Lin, G. (2021). Relationships between above- and below-ground carbon stocks in mangrove forests facilitate better estimation of total mangrove blue carbon. *Carbon Balance and Management*, *16*(1). https://doi.org/10.1186/s13021-021-00172-9

Nascimento, W. R., Souza-Filho, P. W. M., Proisy, C., Lucas, R. M., & Rosenqvist, A. (2013). Mapping changes in the largest continuous Amazonian mangrove belt using object-based classification of multisensor satellite imagery. *Estuarine, Coastal and Shelf Science*, *117*, 83–93. https://doi.org/10.1016/j.ecss.2012.10.005

Navarro, A., Young, M., Allan, B., Carnell, P., Macreadie, P., & Ierodiaconou, D. (2020). The application of Unmanned Aerial Vehicles (UAVs) to estimate above-ground biomass of mangrove ecosystems. *Remote Sensing of Environment*, *242*, 111747. https://doi.org/10.1016/j.rse.2020.111747

Nunes, S. P. D. Q., França, M. C., Cohen, M. C. L., Pessenda, L. C. R., Rodrigues, E. S. F., Magalhães, E. A. S., & Silva, F. A. B. (2023). Assessment the impacts of sea-level changes on mangroves of Ceará-Mirim Estuary, Northeastern Brazil, during the Holocene and Anthropocene. *Plants*, *12*(8), 1721. https://doi.org/10.3390/PLANTS12081721/S1

Osland, M. J., Day, R. H., Larriviere, J. C., & From, A. S. (2014). Aboveground allometric models for freeze-affected black mangroves (*Avicennia germinans*): equations for a climate sensitive mangrove-marsh ecotone. *PLoS ONE*, *9*(6). https://doi.org/10.1371/journal.pone.0099604

Palacios Peñaranda, M. L., Cantera Kintz, J. R., & Peña Salamanca, E. J. (2019). Carbon stocks in mangrove forests of the Colombian Pacific. *Estuarine, Coastal and Shelf Science*, *227*. https://doi.org/10.1016/j.ecss.2019.106299

Pamplona, F. C., Paes, E. T., & Nepomuceno, A. (2013). Nutrient fluctuations in the Quatipuru river: A macrotidal estuarine mangrove system in the Brazilian Amazonian basin. *Estuarine, Coastal and Shelf Science*, *133*, 273–284. https://doi.org/10.1016/j.ecss.2013.09.010

Panagiotidis, D., Abdollahnejad, A., Surový, P., & Chiteculo, V. (2017). Determining tree height and crown diameter from high-resolution UAV imagery. *International Journal of Remote Sensing*, *38*(8–10), 2392–2410. https://doi.org/10.1080/01431161.2016.1264028

Price, C. A., Branoff, B., Cummins, K., Kakaï, R. G., Ogurcak, D., Papeş, M., Ross, M., Whelan, K. R. T., & Schroeder, T. A. (2024). Global data compilation across climate gradients supports the use of common allometric equations for three transatlantic mangrove species. *Ecology and Evolution*, *14*(11). https://doi.org/10.1002/ece3.70577

Price, C. A., Schroeder, T. A., Branoff, B., Van Bloem, S. J., Pillot-Torres, N., Chaudry, M. H., Papeş, M., & Marcano-Vega, H. (2025). Allometric relationships for the linear dimensions and biomass of Puerto Rican mangroves. *Forest Ecology and Management*, *593*. https://doi.org/10.1016/j.foreco.2025.122908

Rizzoli, P., Martone, M., Gonzalez, C., Wecklich, C., Borla Tridon, D., Bräutigam, B., Bachmann, M., Schulze, D., Fritz, T., Huber, M., Wessel, B., Krieger, G., Zink, M., & Moreira, A. (2017). Generation and performance assessment of the global TanDEM-X digital elevation model. *ISPRS Journal of Photogrammetry and Remote Sensing*, *132*, 119–139. https://doi.org/10.1016/j.isprsjprs.2017.08.008

Rosseti, D. F., Trukenbrodt, W., & Góes, A. (1989). Estudo paleoambiental e estratigráfico dos Sedimentos Barreiras e pós-Barreiras na região Bragantina, nordeste do Pará. *Boletim Do Museu Paraense Emílio Goeldi. Série Ciências Da Terra*, 25–74.

Rovai, A. S., Twilley, R. R., Castañeda-Moya, E., Riul, P., Cifuentes-Jara, M., Manrow-Villalobos, M., Horta, P. A., Simonassi, J. C., Fonseca, A. L., & Pagliosa, P. R. (2018). Global controls on carbon storage in mangrove soils. *Nature Climate Change*, *8*(6), 534–538. https://doi.org/10.1038/s41558-018-0162-5

Rovai, A. S., Twilley, R. R., Worthington, T. A., & Riul, P. (2022). Brazilian mangroves: blue carbon hotspots of national and global relevance to natural climate solutions. *Frontiers in Forests and Global Change*, *4*. https://doi.org/10.3389/ffgc.2021.787533

Ruiz Pessenda, L. C., Ribeiro, A. de S., Marques Gouveia, S. E., Aravena, R., Boulet, R., & Bendassolli, J. A. (2004). Vegetation dynamics during the late Pleistocene in the Barreirinhas region, Maranhão State, northeastern Brazil, based on carbon isotopes in soil organic matter. *Quaternary Research*, *62*(2), 183–193. https://doi.org/10.1016/j.yqres.2004.06.003

Saarela, S., Wästlund, A., Holmström, E., Mensah, A. A., Holm, S., Nilsson, M., Fridman, J., & Ståhl, G. (2020). Mapping aboveground biomass and its prediction uncertainty using LiDAR and field data, accounting for tree-level allometric and LiDAR model errors. *Forest Ecosystems*, *7*(1), 43. https://doi.org/10.1186/s40663-020-00245-0

Saatchi, S. S., Harris, N. L., Brown, S., Lefsky, M., Mitchard, E. T. A., Salas, W., Zutta, B. R., Buermann, W., Lewis, S. L., Hagen, S., Petrova, S., White, L., Silman, M., & Morel, A. (2011). Benchmark map of forest carbon stocks in tropical regions across three continents. *Proceedings of the National Academy of Sciences*, *108*(24), 9899–9904. https://doi.org/10.1073/pnas.1019576108

Sanderman, J., Hengl, T., Fiske, G., -, al, Lagomasino, D., Fatoyinbo, T., Lee, S., Feliciano, E., Trettin, C., Shapiro, A., & Mangora, M. M. (2019). *Measuring mangrove carbon loss and gain in deltas*. https://doi.org/10.1088/1748-9326/aaf0de

Sanderman, J., Hengl, T., Fiske, G., Solvik, K., Adame, M. F., Benson, L., Bukoski, J. J., Carnell, P., Cifuentes-Jara, M., Donato, D., Duncan, C., Eid, E. M., Ermgassen, P. Z., Lewis, C. J. E., Macreadie, P. I., Glass, L., Gress, S., Jardine, S. L., Jones, T. G., … Landis, E. (2018). A global map of mangrove forest soil carbon at 30 m spatial resolution. *Environmental Research Letters*, *13*(5). https://doi.org/10.1088/1748-9326/aabe1c

Silva, 1998. Análise morfoestratigráfica do estuário do rio Marapanim- NE do Pará. Orientador: Maâmar El-Robrini. Dissertação, Geologia e Geoquímica, Centro de Geociências, Universidade Federal do Pará, Belém, 133 p.

Silva, C. A. da, Souza-Filho, P. W. M., & Rodrigues, S. W. P. (2009). Morphology and modern sedimentary deposits of the macrotidal Marapanim Estuary (Amazon, Brazil). *Continental Shelf Research*, ***29***(3): 619–631. https://doi.org/10.1016/j.csr.2008.09.018

Simard, M., Fatoyinbo, L., Smetanka, C., Rivera-Monroy, V. H., Castañeda-Moya, E., Thomas, N., & Van der Stocken, T. (2019). Mangrove canopy height globally related to precipitation, temperature and cyclone frequency. *Nature Geoscience*, *12*(1), 40–45. https://doi.org/10.1038/s41561-018-0279-1

Simard, M., Fatoyinbo, L., Thomas, N. M., Stovall, A. E., Parra, A., Barenblitt, A., Bunting, P., & Hajnsek, I. (2025). A new global mangrove height map with a 12 meter spatial resolution. *Scientific Data* , *12*(1). https://doi.org/10.1038/s41597-024-04213-z

Simard, M., Pinto, N., Fisher, J. B., & Baccini, A. (2011). Mapping forest canopy height globally with spaceborne lidar. *Journal of Geophysical Research: Biogeosciences*, *116*(4). https://doi.org/10.1029/2011JG001708

Simard, M., Zhang, K., Rivera-Monroy, V. H., Ross, M. S., Ruiz, P. L., Castañeda-Moya, E., Twilley, R. R., & Rodriguez, E. (2006). Mapping height and biomass of mangrove forests in everglades national park with SRTM elevation data. *Photogrammetric Engineering & Remote Sensing*, *72*(3), 299–311. https://doi.org/10.14358/PERS.72.3.299

Singha, C., & Swain, K. C. (2022). Quantifying changes in sundarbans mangrove forest through gee cloud computing approach (pp. 113–129). https://doi.org/10.1007/978-981-19-0332-8_9

Spalding, M. D., Leal, M., Ahmadia, G. N., Aigrette, L., Andradi-Brown, D. A., Arquiza, Y., Balidy, H., Bandeira, S., Beck, M. W., Beeston, M., Beyeler, J., Brana-Varela, J., Bresnahan, M., Bunting, P., Calzada Vazquez Vela, A., Camacho, J., Roy Chowdhury, M., Connolly, R., Dahdouh-Guebas, F., … zu Ermgassen, P. (2021). The state of the world's mangroves 2021.

Spivak, A. C., Sanderman, J., Bowen, J. L., Canuel, E. A., & Hopkinson, C. S. (2019). Global-change controls on soil-carbon accumulation and loss in coastal vegetated ecosystems. *Nat Geosci*, *12*(9), 685–692. https://doi.org/10.1038/s41561-019-0435-2

Stovall, A. E. L., Fatoyinbo, T., Thomas, N. M., Armston, J., Ebanega, M. O., Simard, M., Trettin, C., Obiang Zogo, R. V., Aken, I. A., Debina, M., Me Kemoe, A. M., Assoumou, E. O., Kim, J. S., Lagomasino, D., Lee, S.-K., Ndong Obame, J. C., Voubou, G. D., & Essono, C. Z. (2021). Comprehensive comparison of airborne and spaceborne SAR and

LiDAR estimates of forest structure in the tallest mangrove forest on earth. *Science of Remote Sensing*, *4*, 100034. https://doi.org/10.1016/j.srs.2021.100034

Suárez, N., Medina, E. Salinity effect on plant growth and leaf demography of the mangrove, *Avicennia germinans* L.. *Trees* 19, 722–728 (2005). https://doi.org/10.1007/s00468-005-0001-y

Suresh, A., & Soon Park, J. (2018). Blue Carbon Stock of Mangrove Ecosystems. *International Journal of Science and Research*. https://doi.org/10.21275/ART20203497

Trettin, C. C., Dai, Z., Tang, W., Lagomasino, D., Thomas, N., Lee, S. K., Simard, M., Ebanega, M. O., Stoval, A., & Fatoyinbo, T. E. (2021). Mangrove carbon stocks in Pongara National Park, Gabon. *Estuarine, Coastal and Shelf Science*, *259*, 107432. https://doi.org/10.1016/J.ECSS.2021.107432

Vilhena, M. D. P. S. P., Costa, M. L. Da, & Berrêdo, J. F. (2010). Continental and marine contributions to formation of mangrove sediments in an Eastern Amazonian mudplain: The case of the Marapanim Estuary. *Journal of South American Earth Sciences*, *29*(2), 427–438. https://doi.org/10.1016/j.jsames.2009.07.005

Wang, D., Wan, B., Qiu, P., Zuo, Z., Wang, R., & Wu, X. (2019). Mapping height and aboveground biomass of mangrove forests on Hainan Island using UAV-LiDAR Sampling. *Remote Sensing*, *11*(18), 2156. https://doi.org/10.3390/rs11182156

Wang, F., Cheng, P., Chen, N., & Kuo, Y.-M. (2021). Tidal driven nutrient exchange between mangroves and estuary reveals a dynamic source–sink pattern. *Chemosphere*, 270, 128665. https://doi.org/10.1016/j.chemosphere.2020.128665

Wessel, B., Huber, M., Wohlfart, C., Marschalk, U., Kosmann, D., & Roth, A. (2018). Accuracy assessment of the global TanDEM-X Digital Elevation Model with GPS data. *ISPRS Journal of Photogrammetry and Remote Sensing*, *139*, 171–182. https://doi.org/10.1016/j.isprsjprs.2018.02.017

Woodroffe, C. D., Rogers, K., McKee, K. L., Lovelock, C. E., Mendelssohn, I. A., & Saintilan, N. (2016). Mangrove sedimentation and response to relative sea-level rise. *Annual Review of Marine Science*, *8*, 243–266. https://doi.org/10.1146/annurev-marine-122414-034025

Xiong, L., Lagomasino, D., Charles, S. P., Castañeda-Moya, E., Cook, B. D., Redwine, J., & Fatoyinbo, L. (2022). Quantifying mangrove canopy regrowth and recovery after Hurricane Irma with large-scale repeat airborne lidar in the Florida Everglades. *International Journal of Applied Earth Observation and Geoinformation*, *114*. https://doi.org/10.1016/j.jag.2022.103031

Xu, X., Wang, J., Wang, Y., & Kokhanovsky, A. (2018). Passive remote sensing of aerosol height. *Remote Sensing of Aerosols, Clouds, and Precipitation*, 1–22. https://doi.org/10.1016/B978-0-12-810437-8.00001-3

Zaman, M. R., Rahman, M. S., Ahmed, S., & Zuidema, P. A. (2023). What drives carbon stocks in a mangrove forest? the role of stand structure, species diversity and functional traits. *Estuarine, Coastal and Shelf Science*, *295*. https://doi.org/10.1016/j.ecss.2023.108556

Zanne, A. E., Lopez-Gonzalez, G., Coomes, D. A., Ilic, J., Jansen, S., Lewis, S. L., Miller, R. B., Swenson, N. G., Wiemann, M. C., & Chave, J. (2009). *Data from: towards a worldwide wood economics spectrum* [Dataset]. Dryad. https://doi.org/10.5061/dryad.234

Zhang, K., Liu, H., Li, Y., Xu, H., Shen, J., Rhome, J., & Smith, T. J. (2012). The role of mangroves in attenuating storm surges. *Estuarine, Coastal and Shelf Science*, *102–103*, 11–23. https://doi.org/10.1016/j.ecss.2012.02.021